Contents lists available at ScienceDirect

Chemical Engineering Research and Design

journal homepage: www.elsevier.com/locate/cherd

Ultrasonic enhanced adsorption of methylene blue onto the optimized surface area of activated carbon: Adsorption isotherm, kinetics and thermodynamics

T.C. Egbosiuba[a,d,e,*], A.S. Abdulkareem[a,e], A.S. Kovo[a,e], E.A. Afolabi[a], J.O. Tijani[b,e], M. Auta[a], W.D. Roos[c]

[a] Department of Chemical Engineering, Federal University of Technology, PMB.65, Minna, Niger State, Nigeria
[b] Department of Chemistry, Federal University of Technology, PMB.65, Minna, Niger State, Nigeria
[c] Department of Physics, University of the Free State, P.O. Box 339, ZA-9300 Bloemfontein, South Africa
[d] Department of Chemical Engineering, Chukwuemeka Odumegwu Ojukwu University, Uli Campus, Anambra State, Nigeria
[e] Nanotechnology Research Group, Centre for Genetic Engineering and Biotechnology (CGEB), Federal University of Technology, P.M.B 65, Bosso, Minna, Niger State, Nigeria

ARTICLE INFO

Article history:
Received 14 June 2019
Received in revised form 6 October 2019
Accepted 9 October 2019
Available online 19 October 2019

Keywords:
Empty fruit bunch
Response surface methodology
Ultrasonication
Activated carbon
Methylene blue
Adsorption

ABSTRACT

In this study, the influence of pyrolysis time and temperature on yield, fixed carbon and physicochemical properties of the biochar produced from Empty Fruit Bunch (EFB) were investigated. Response Surface Methodology was utilized to optimize the influence of process parameters on the surface area of activated carbon produced from the biochar in the absence and presence of ultrasonication and was coded EFB-AC and EFB-UAC respectively. The EFB-AC and EFB-UAC were characterized using BET, TGA, HRSEM, XRD, FTIR and XPS. The batch adsorption behavior of MB onto EFB-AC and EFB-UAC was evaluated. The results revealed that the optimum surface area (S_{BET}) of 2114 m^2/g was achieved for EFB-UAC at activation temperature (600 °C), activation time (45 min) and KOH concentration (1.5 M). It was found that EFB-UAC has high surface area, better thermal stability, better pores development and improved surface chemistry compared to the EFB-AC. The maximum adsorption of MB occurred at pH (10), adsorbent dosage (30 mg), contact time (40 min), Temperature (50 °C) and MB initial concentration (50 mg/L). The experimental data was best described by Langmuir isotherm model, having an adsorption capacity of 400 mg/g and 435 mg/g for EFB-AC and EFB-UAC, respectively. The kinetic model was best suited by pseudo-second order model for MB adsorption onto EFB-AC and EFB-UAC. The thermodynamics investigation showed that adsorption of MB was endothermic in nature due to strong electrostatic interaction and formation of hydrogen bonding. The study revealed that ultrasonic assisted variations of the adsorption parameters significantly improved the adsorption of MB onto EFB-AC and EFB-UAC.

Abbreviations: EFB, empty fruit bunch; EFB-UAC, ultrasonic enhanced empty fruit bunch activated carbon; EFB-UAC, empty fruit bunch activated carbon produced without ultrasonication; MB, methylene blue; MC, moisture content; RSM, response surface methodology; CCD, central composite design; BET, Brunauer–Emmett–Teller; TGA, thermogravimetric analysis; HRSEM, high resolution scanning electron microscopy; XRD, X-ray diffraction; FTIR, fourier transform infrared; XPS, X-ray photoelectron spectroscopy; ANOVA, analysis of variance; DF, degree of freedom; ASTM, American Society for Testing and Materials; VM, volatile matter; EDS, energy dispersive spectrometer; pH_{PZC}, point of zero charge; R^2, coefficient of determination; SSE, sum of Square Error; χ^2, Chi-Square Test; PFO, pseudo-first order; PSO, pseudo-second order; IPD, intraparticle diffusion; A, activation temperature; B, activation time; C, KOH concentration.

* *Corresponding author at*: Department of Chemical Engineering, Chukwuemeka Odumegwu Ojukwu University, Uli Campus, Anambra State, Nigeria.
E-mail addresses: egbosiubachinedu@gmail.com, ct.egbosiuba@coou.edu.ng (T.C. Egbosiuba).
https://doi.org/10.1016/j.cherd.2019.10.016
0263-8762/

1. Introduction

The global utilization of pigments and dyes in chemical industries for instance paper, textiles, plastic, printing, food, pharmaceutical, cosmetics and rubber industries have been widely recognized and documented (Fakhri et al., 2017; Lima et al., 2019). The effluents generated from these industries affects the environment and human body adversely (Ibupoto et al., 2018). About 10% of the hundred thousand tons of produced dyes in these industries are discharged into the environment as wastewater (Marrakchi et al., 2017). Basically, synthetic dyes unlike natural dyes exhibit molecular stability and are classified as cationic, anionic and non-ionic dyes because of their charge (Li et al., 2019). Methylene blue (MB), is a commonly used cationic dye and a major constituent of wastewater from these industries (Wang et al., 2018b; Yang et al., 2019). Previous studies have revealed that exposure to MB can cause eye injuries and skin damage, while high heart rate, digestive disorder, nausea, vomiting and tissue necrosis are due to direct ingestion of MB (Banerjee et al., 2017; Konicki et al., 2017; Wang et al., 2018a). Therefore, development of an efficient and advanced treatment method for the removal of MB from wastewater is considered important in order to maintain a safe and healthy environment.

Several attempts have been made to remove MB using physical treatment such as filtration (Yang et al., 2019), reverse osmosis (Qasim et al., 2019), flocculation (Suresh et al., 2018) and coagulation (Pinto et al., 2019), chemical treatments; which include photodegradation (Jiang et al., 2018) and photo-Fenton (Hodaifa et al., 2019), and biological treatments via anaerobic or aerobic biodegradation (Gaur et al., 2018). However, these methods possessed some environmental and economic drawbacks which include generation of secondary pollutants, high cost, operations delay, complex treatment techniques, inadequate removal efficiency and oxidizing agents dependence (Charola et al., 2019; Li et al., 2017a,b). On the contrary, adsorption technology has been identified as a superior alternative treatment method due to its low cost, efficiency, ease of operation conditions, adsorbents diversity, inertness to materials and environmentally friendly compared to other treatment techniques (Guo et al., 2019; Konicki et al., 2018; Tian et al., 2018; Zhang et al., 2016). Activated carbon remains one of the most investigated adsorbents by researchers due to its porous structure, high surface area, abundance of surface functional groups and high adsorption capacity (Altıntıg et al., 2017; Kluczka et al., 2019). However, the production cost of commercial activated carbon is high hence underutilized agricultural wastes have been identified as a viable feedstock substitute to produce cost effective activated carbon.

Researchers have exploited different renewable and low agricultural byproducts namely; rice husk (Menya et al., 2017), mustard husk (Charola et al., 2019), almond shell (Zbair et al., 2018), sunflower (Moralı et al., 2018), coconut shell (Islam et al., 2017), acorn shell (Altıntıg et al., 2017), pecan nut shell (Lima et al., 2019), peanut shell (Cai et al., 2018), corn bract (Lin et al., 2018) and walnut shell (Miyah et al., 2018) amongst others to produce activated carbon. In this study, Empty Fruits Bunches from Palm tree was used to produce activated carbon. It is interesting to note that the global production capacity of oil palm is 75.51 million MT and Indonesia (43.00 million MT), Malaysia (20.70 million MT), Thailand (3.00 million MT), Colombia (1.68 million MT) and Nigeria (1.02 million MT) are the leading producers (USDA, 2019).

Specifically, Nigeria is known to be one of the leading producers of oil palm. Unfortunately, the processing of oil palm to produce palm oil generates enormous quantity of wastes such as palm kernel shells (6%), mesocarp fibres (15%) and empty fruit bunches (EFB) (23%) in a ton fresh fruit bunch of oil palm. At the moment, there is a growing concern over the indiscriminate disposal of EFB into the environment, which constitute a great danger to public health (Liew et al., 2017). Not only that the indiscriminate burning of oil palm wastes in boiler for steam production also causes air pollution and release of harmful gases into the atmosphere. In addition, the utilization of oil palm wastes as a combustion material for electricity also produces undesirable ash. This necessitates the conversion of lost cost EFB into useful product like activated carbon that can remove undesirable pollutants from industrial wastewater that would be of benefit to the environment and the scientific community in the search for cheaper adsorbent material.

Furthermore, different techniques among which is pyrolysis have been identified as one of the most reliable thermochemical process for the conversion of solid waste feedstock to high value biochar (Morin et al., 2018). Pyrolysis is usually carried out in the absence of oxygen depending on the applied temperature and heating rate (Chen et al., 2018). However, slow pyrolysis often leads to high yield of biochar that is rich in carbon content with an aromatic structure containing oxygen. The large quantity of oxygen rich surface functional groups of biochars enhances their chemical activation for different applications (Lee et al., 2017). Several authors have reported the modification of the properties of biochar by acids, bases, steam, metal oxides, clay minerals, carbonaceous materials and organic compounds to enhance its surface area and porosity (Ait Ahsaaine et al., 2018; Zbair et al., 2018).

Response surface method (RSM) has been recognized as a tool that revealed the interaction among two or more of the process parameters. Different researchers have employed RSM to optimize the experimental variables in the preparation of activated carbon from agricultural feed stocks such as mustard husk (Charola et al., 2019), peanut shells (Xu et al., 2017), tobacco stem (Yu et al., 2019), rice husk (Zhang et al., 2017), almond shell (Zbair et al., 2018), coconut shell (Dissanayake Herath et al., 2019), Africana seed hulls (Garba and Rahim, 2014), cassava stem (Sulaiman et al. 2018). However, most of these studies did not investigate the influence of ultrasonication on the optimization of the experimental conditions. Ultrasonication is a process that enhances mass transfer through utilization of sound waves to generate fluctuations in pressure within aqueous medium which resulted to the growth, formation and eventual collapse of microbubbles in microseconds. The sonication effect also lead to micro-explosions under high pressure and temperature (Sodeifian and Ali, 2018). To the best of our knowledge, the optimization of the influence of process parameters on the surface area of developed activated carbon from EFB via RSM technique under ultrasonic effect has not been investigated. Thus, the present study focused on the preparation of activated carbon from EFB via ultrasonic assisted optimization of temperature, time and KOH concentration to produce material with high surface area and adsorption capacity for MB molecules. Furthermore, statistical approach of Design of Experiment (DOE) using RSM was adapted for Empty Fruits Bunch-Ultrasonicated Activated Carbon (EFB-UAC) preparation to determine the parameters with the most impact on the surface area of the activated carbon. The prepared EFB-AC and EFB-UAC were characterized using several analytical techniques. This was followed by the investigation of the ultrasonic assisted adsorption behavior of EFB-AC and EFB-UAC for the removal of MB from aqueous solution via batch process.

2. Materials and methods

2.1. Materials

Analytical grade sodium hydroxide (NaOH), potassium hydroxide (KOH), hydrochloric acid (HCl) and MB ($C_{16}H_{18}ClN_3S^*H_20$, MW = 319.86 G/mol) with percentage purity in the range of 95–99.9% used were obtained from Sigma Aldrich. The chemicals/reagents were used as received without further purification. The nitrogen gas (95–99.9%) used in this study was purchased from Vinee Gas Ltd. Abuja, Nigeria.

2.2. Samples collection and pre-treatment

The EFB feed stocks were randomly collected from different locations within Neni, Anambra State. The EFB wastes were washed with distilled water to remove possible impurities followed by oven dried overnight at 105 °C to remove residual water. The oven dried sample was subjected to size reduction and sieved with a 500 μm sieve. The powdered EFB was subjected to then thermogravimetric analysis (TGA) as well as

proximate and ultimate analysis prior to pyrolysis to obtain the best degradation temperature profile.

2.3. Optimization of EFB pyrolysis

Six (6) crucibles each containing 20 g of powdered EFB was subjected to slow pyrolysis at different times and temperatures in the furnace shown in Fig. 1. The horizontal tubular furnace was set at a heating rate of 10 °C/min, and N_2 flow rate of 60 mL/min. The pyrolysis temperatures used were in the range 300 °C–500 °C and the time was either 30 or 60 min (Table 2). After each pyrolysis conditions, the sample was removed and the yield of biochar calculated using Eq. (1).

$$\text{Yield}_{\text{biochar}}\,(\%) = \frac{Mass_{biochar}}{\text{Mass}_{\text{raw EFB}}} \times 100\,\% \tag{1}$$

where $\text{Yield}_{\text{biochar}}$ (%) is the mass yield of biochar after pyrolysis, $\text{Mass}_{\text{biochar}}$ (g) $\text{Mass}_{\text{biochar}}$ (g) is the mass of biochar and $\text{Mass}_{\text{raw EFB}}$ refers to the mass of raw biomass.

2.4. Optimization of chemical activation of EFB biochar

Chemical activation of biochar obtained from EFB was performed to investigate the influence of ultrasonic assisted effects of the parameters of activation process such as temperature, activation time and KOH concentration on the activated carbon surface area. The values of the activation parameters utilized in this study were obtained through the preliminary investigation carried out using the range of values from the literature. The considered levels and values of the activation parameters are presented in Table 1a using adopted Central Composite Design (CCD).

Biochar (5 g) was soaked with 100 mL of 2 M KOH in a 200 cm^3 conical flask and sonicated for 1 h at 40 °C. The sample was later poured into a crucible and calcined in the furnace at 500 °C for 60 min and thereafter cooled to room temperature and stored in an air tight container. The surface area of produced activated carbon was determined by Nitrogen adsorption–desorption Brunauer–Emmett–Teller (BET) technique. The same procedure was repeated for other experimental runs using the applied conditions as presented in Table 1b. The obtained activated carbon was designated as EFB-UAC. Similarly, the activated carbon labeled as EFB-AC was produced using the optimum conditions of activation process (Temp. = 600 °C, time = 45 min, KOH conc. = 1.5 M), but without ultrasonic influence.

2.5. Proximate and ultimate analysis

The raw EFB and the produced biochar at different temperatures and times were characterized to determine the volatile matter content, ash content, moisture content and fixed carbon content. The moisture content of the samples was determined using ASTM D2867 – 09 standard test method. The sample (10 g) each of raw EFB and biochar was placed into a crucible of a known weight, weighed accurately and was placed with the lid inside the oven. The EFB sample was dried at 105 °C for 2 h and was allowed to cool to room temperature before being removed from the oven. The final weight of the samples was also determined and recorded. The moisture content (MC) of the sample was expressed in terms of percentage difference of weight using Eq. (2).

$$\text{MC (wt\%)} = \frac{w_1 - w_2}{w_1 - w_0} \times 100\,\% \tag{2}$$

where w_0 = crucible weight, w_1 = crucible weight + EFB sample before incineration and w_2 = crucible weight + EFB sample after incineration.

The percentage of volatile matter of the raw EFB and biochar samples was obtained using the ASTM D5832 – 98 standard test methods. A known mass (10 g) each of the sample was weighed into a crucible of known mass and placed in muffle furnace regulated to 600 °C for 30 min. On completion, the sample was cooled to room temperature and the mass of the crucible with the sample after incineration was recorded. The percentage mass loss (volatile matter (VM)) was calculated using Eq. (3).

$$\text{VM (wt\%)} = \frac{w_i - w_f}{w_i} \times 100\,\% \tag{3}$$

where w_i is the initial sample mass prior to incineration while w_f is the final sample mass after incineration.

The ash content determination was carried out using the ASTM D2866 – 94 standard test method in a muffle furnace. A known mass of raw EFB (10 g) and biochar sample mass (10 g) was weighed and poured into a crucible of mass, (w_a). The crucible containing the samples was placed in the muffle furnace and maintained at 800 °C for 1 h and thereafter allowed to cool to room temperature and re-weighed. The percentage ash content (Ash) was calculated using Eq. (4).

$$\text{Ash (wt\%)} = \frac{w_c - w_a}{w_b - w_a} \times 100\,\% \tag{4}$$

where w_a is the mass of the crucible, w_b is the mass of the crucible and the sample prior to incineration and w_c is the mass of the crucible and the sample after incineration.

Fixed carbon content was obtained using Eq. (5).

$$\text{Fixed carbon (wt\%)} = 100 - (\text{MC (wt\%)} + \text{VM (wt\%)} + \text{Ash (wt\%)}) \tag{5}$$

The elemental content namely; carbon, nitrogen, hydrogen and sulfur of the pyrolytic feedstock (EFB) and the produced biochar was determined using Perkin Elmer Elemental Analyzer (Model 240C). The value of oxygen content was obtained using Eq. (6).

$$\text{Oxygen (wt\%)} = 100 - (\text{carbon (wt\%)} + \text{nitrogen (wt\%)} + \text{hydrogen (wt\%)} + \text{sulfur (wt\%)}) \tag{6}$$

2.6. Characterization of EFB-AC and EFB-UAC

The thermal profiles of raw EFB, EFB-AC and EFB-UAC were examined using TGA 4000 (Perkin Elmer, UK) operated in the temperature range 30 °C–700 °C with a heating rate of 10 °C/min in a nitrogen environment. Fourier transform infrared spectrometry (FTIR) analysis (Frontier FT-IR, Perkin Elmer, UK) was utilized for the chemical functional group determination of the samples. The morphology and elemental

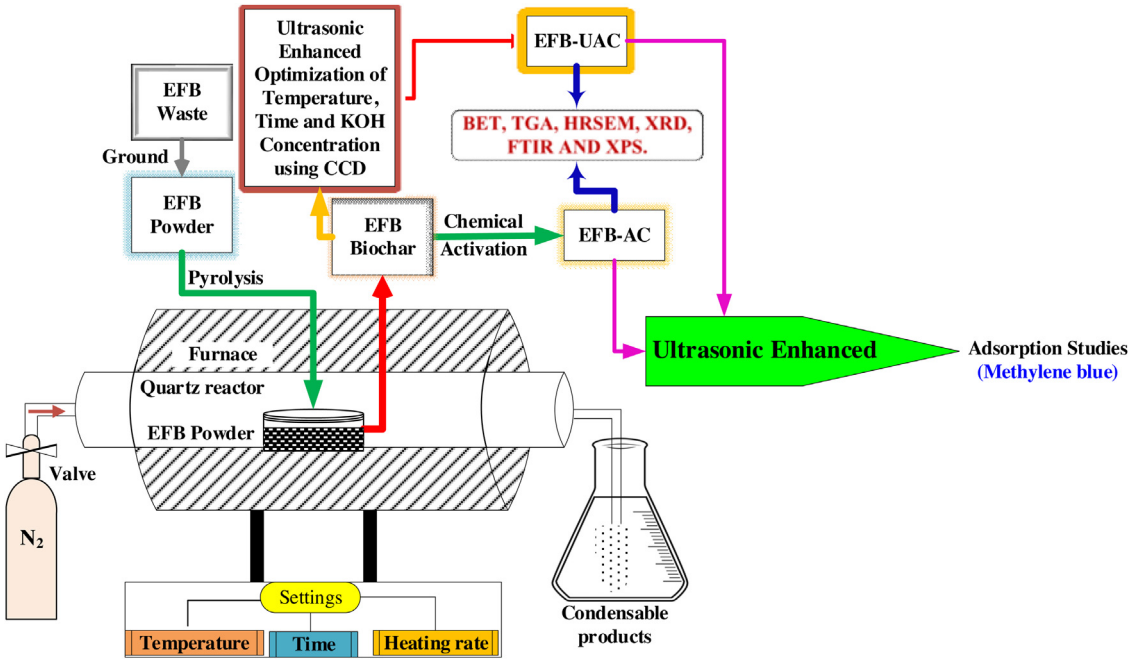

Fig. 1 – The schematic illustration of all experimental procedure.

Table 1 – (a) Actual and coded values of RSM optimization of process parameters for ultrasonic assisted activation of EFB-UAC and (b) detailed experimental run for the ultrasonic enhanced optimization of the surface area of EFB-UAC.

a.

Process parameters	Code	Coded values				
		−α	−1	0	+1	+α
Activation temperature (°C)	A	432	500	600	700	768
Activation time (min)	B	20	30	45	60	70
Activating agent Conc. (M)	C	0.66	1	1.5	2	2.34

b.

Run	Activation temperature (°C)	Activation time (min)	KOH concentration (M)
1(FC)	500	60	2
2(FC)	500	30	1
3(FC)	500	30	2
4(FC)	500	60	1
5(FC)	700	30	1
6(FC)	700	60	2
7(FC)	700	60	1
8(FC)	700	30	2
9(AP)	431.82	45	1.5
10(AP)	768.18	45	1.5
11(AP)	600	19.77	1.5
12(AP)	600	70.23	1.5
13(AP)	600	45	0.66
14(AP)	600	45	2.34
15(CP)	600	45	1.5
16(CP)	600	45	1.5
17(CP)	600	45	1.5
18(CP)	600	45	1.5
19(CP)	600	45	1.5
20(CP)	600	45	1.5

FC = Factorial, AP = Axial Point and CP = Center Point.

compositions of EFB-AC and EFB-UAC carbon was characterized using high resolution scanning electron microscopy (HRSEM) (Zeiss Auriga) with an attached energy dispersive spectrometer (EDS). Surface area of the EFB-AC and EFB-UAC were determined using BET (NOVA4200e, Quantachrome UK). X-ray diffraction (XRD) analysis was carried out to identify the phase structure and the degree of graphitization of the EFB-AC and EFB-UAC using XRD 6000 (Shimadzu Scientific). A PHI 5400 XPS spectrometer was applied to examine the oxidation states and surface functional groups of the prepared material.

Table 2 – The effect of temperature and time on EFB biochar yield, proximate and ultimate analysis.

Temperature (°C)	Time (min)	EFB biochar Yield (wt%)	Proximate analysis				Ultimate analysis			
			MC (wt%)	VM (wt%)	ASH (wt%)	FC (wt%)	C (wt%)	H (wt%)	N (wt%)	O (wt%)
300	30	60.00	8.20	54.80	5.00	32.00	60.17	8.65	0.60	30.58
	60	55.00	6.50	51.50	5.70	36.30	61.26	8.00	0.78	29.96
350	30	57.00	5.00	50.30	6.50	38.20	62.38	7.36	0.85	29.41
	60	53.00	4.60	45.40	7.00	43.00	65.91	6.50	0.98	26.61
400	30	55.50	4.30	37.00	8.20	50.50	67.00	6.20	0.91	25.89
	60	48.40	3.20	35.40	9.60	51.80	72.70	5.00	0.97	21.33
450	30	51.00	2.60	32.80	10.00	54.60	73.29	4.62	1.00	21.09
	60	47.00	2.20	32.70	11.00	54.10	76.58	3.94	1.02	18.46
500	30	48.50	2.00	30.00	11.80	56.20	78.31	2.45	1.16	18.08
	60	45.00	1.80	25.20	12.60	60.40	81.46	1.50	1.21	15.83

2.7. *Ultrasonic assisted batch adsorption studies*

The adsorption experiments of MB onto EFB-UAC were performed using a batch method where the effects of parameters such as adsorbent dosage, contact time, temperature, pH and initial MB concentration on MB adsorption were investigated. Ultrasonic bath (SB25-12DT, Ultrasonic Scientz) was utilized to conduct all the adsorption experiments and the heating system was set at the temperature (40 °C), power (180 W) and frequency (40 kHz), respectively. The procedures are explained as follows.

2.7.1. *Ultrasonic assisted effect of adsorbent dosage*

The ultrasonic assisted influence of adsorbent dosage on MB adsorption was determined by addition of different quantities of EFB-AC and EFB-UAC adsorbent (10, 20, 30, 40, 50 and 60 mg) into 50 cm^3 of the MB solution in a 200 cm^3 conical flask. The covered flask was placed in the ultrasonic bath set at 30 °C while maintaining a constant contact time (20 min) and pH (6). After 20 min of ultrasonication at the different MB concentration (50, 100, 150 and 200 mg/L), the sample was filtered and the filtrate analyzed using UV–vis spectrophotometer (Shimadzu, 84000S) method. The amount of MB adsorbed was calculated using Eq. (7).

2.7.2. *Ultrasonic assisted effect of contact time*

The ultrasonic assisted effect of contact time on the rate of removal of MB by EFB-AC and EFB-UAC was studied with the addition of 30 mg of the adsorbent into 50 cm^3 of MB solution in a conical flask of 200 cm^3. The flask was covered and placed in the ultrasonic bath set at 30 °C for the different contact time (5, 10, 20, 30, 40, 60, 120 and 180 min) at pH of 6. After each contact time of ultrasonication at the different MB concentration (50, 100, 150 and 200 mg/L), the sample was filtered and the filtrate analyzed using UV–vis spectrophotometer method. The adsorbed amount of MB was calculated using Eq. (7).

2.7.3. *Ultrasonic assisted effect of temperature*

The ultrasonic assisted influence of temperature on the amount of MB adsorbed was determined by adding 30 mg of the adsorbent to 50 cm^3 of MB solution in a 200 cm^3 conical flask and placed in the ultrasonic bath. The flask was properly covered and the temperature was varied at 25, 30, 35, 40, 45 and 50 °C using a constant equilibrium contact time (40 min) and pH (6). As the required contact time was attained using different MB concentration (50, 100, 150 and 200 mg/L), the sample was filtered for residue removal while the filtrate was characterized using UV–vis spectrophotometer method. The amount of MB adsorbed was calculated using Eq. (7).

2.7.4. *Ultrasonic assisted effect of pH*

The ultrasonic assisted influence of pH on the adsorbed quantity of MB was studied at the pH (2, 3, 4, 5, 6, 8, 10) using either 0.1 M HCl or 0.1 M NaOH at a constant adsorbent dosage (30 mg), contact time (40 min) and temperature (50 °C). A known mass (30 mg) of the adsorbent was added to 50 cm^3 of MB solution in a 200 cm^3 conical flask and placed in the ultrasonic bath. The sample was filtered to remove the residue and the filtrate characterized for MB using UV–vis spectrophotometer and recorded. The amount of MB adsorbed was computed using Eq. (7).

2.7.5. *Ultrasonic assisted effect of initial MB concentration*

The ultrasonic assisted influence of MB initial concentration on the rate of MB removal by the adsorbents were investigated by adding 30 mg of the adsorbent (EFB-AC, EFB-UAC) into 50 cm^3 of MB solution in a 200 cm^3 conical flask. The covered flask was placed in the ultrasonic bath and operated for various initial MB concentration (50, 100, 150 and 200 mg/L) at a constant adsorbent dosage (30 mg), contact time (40 min), temperature (50 °C) and pH (10). The solution was filtered and the filtrate analyzed using UV-vis spectrophotometer. The amount of MB adsorbed was calculated using Eq. (7).

2.7.6. *Determination of point of zero charge (pH_{PZC}) of EFB-AC and EFB-UAC*

The point of zero charge (pH_{PZC}) which is expressed as the electrical balance between the adsorbent surface and MB solution was determined. 100 mL of MB solution was poured into 10 different Erlenmeyer flasks and the initial pH (pH_i) was maintained for each flask in the range of 2–10 (at 1.0 intervals). Few drops of 1.0 M of HCl or NaOH was added to the mixture and the pH of the solution was determined using a pH meter (Eutech Instruments, Model Ecoscan Singapore). The determined optimum dosage (30 mg) of EFB-AC was added into the 10 flasks and placed on a shaker for 48 h to achieve balance charges between the surface of the adsorbent and MB solution. The suspension was filtered after 48 h and the final pH at equilibrium (pH_f) of the filtrate was noted. The pH_{PZC} is the intersection point between the curve of pH_i against pH_f and identity function $pH_i = pH_f$. Similarly, same experimental procedure was performed for the point zero charge (pHzpc) determination of EFB-UAC.

2.7.7. Determination of ionic strength on MB adsorption

The ionic strength effect on MB removal by the EFB-AC and EFB-UAC was carried out by adding NaCa in the concentration range of 0.1–1.0 mol/L into MB solution of 100 mg/L at the temperature (50 °C), adsorbent dosage (30 mg), contact time (40 min) and solution pH (10).

2.7.8. Regeneration studies

The reusability of the EFB-AC and EFB-UAC as an adsorbent was evaluated. In this case, 0.1 M NaOH solution was used as a medium to desorb the adsorbed MB dye on the surface of the adsorbent. A known quantity (50 mg) of the MB adsorbed EFB-AC and EFB-UAC was added into 50 cm^3 of 0.1 M NaOH solution followed by continuous stirring at room temperature of 45 min. The regenerated EFB-AC and EFB-UAC was washed severally with deionized water for efficient removal of desorbing species. Subsequently, the regenerated adsorbents was mixed with 0.1 M HCl and reused for 5 cycles of adsorption to determine its effectiveness and stability.

2.8. Data analysis

The amount of MB adsorbed at equilibrium and the percentage removal were calculated by the following equations:

$$q_{e,t} = \frac{(C_0 - C_{e,t})\,V}{m} \tag{7}$$

$$\text{Removal}\,\% = \frac{C_0 - C_{e,t}}{C_0} \times 100 \tag{8}$$

where $q_{e,t}$ (mg/g) is the adsorption capacity of MB adsorbed per gram of the adsorbent at equilibrium, C_0 (mg/L) = the initial concentrations of MB and $C_{e,t}$ (mg/L) = equilibrium concentrations of MB, m (g) = the adsorbent weight and V (L) = the adsorbate solution volume.

2.8.1. Adsorption isotherm models

To evaluate the distribution of adsorbate molecules at solid/liquid interface, some adsorption isotherm models were applied. The obtained equilibrium adsorption data in this work was analyzed using Langmuir (Langmuir, 1918), Freundlich (Wang et al., 2018c), Temkin isotherm (Danish et al., 2018b) and Dubinin–Radushkevich (D–R) (Dubinin, 1969) models to indicate MB adsorption onto the surface of EFB-AC and EFB-UAC adsorbents.

The Langmuir isotherm model is mathematically represented by the equation:

$$\frac{C_e}{q_e} = \frac{1}{K_L q_m} + \frac{C_e}{q_m} \tag{9}$$

Freundlich isotherm model equation is described as follows:

$$\text{In}q_e = \text{In}\,K_F + \frac{1}{n_F}\text{In}C_e \tag{10}$$

Temkin isotherm model equation is represented as follows:

$$q_e = \frac{RT}{b_T}\text{In}A_T + \left(\frac{RT}{b_T}\right)\text{In}C_e \tag{11}$$

D–R model is mathematically represented in the following equation:

$$\text{In}\,q_e = \text{In}q_s - k_{ad}\varepsilon^2 \tag{12}$$

where q_e (mg/g) is the quantity of MB adsorbed at equilibrium, q_m (mg/g) represents maximum adsorption capacity for monolayer coverage on the surface of adsorbent, C_e (mg/L) depicts MB concentration at equilibrium. k_L (L mg^{-1}) is the Langmuir equilibrium adsorption constant. K_F (mg/g) and n_F = the Freundlich adsorption isotherm constant denoting the adsorption capacity of the EFB-UAC and the heterogeneity of adsorption process respectively. b_T (kJ/mol) and A_T (L/g) = Temkin constants that are related to the heat of adsorption and maximum binding energy. T = temperature (°C), while R (8.314 J/mol.K) = universal gas constant. q_{ad} and q_s = constant related to adsorption mean free energy and D–R adsorption capacity at monolayer saturation, while ε is a Polyani potential.

2.8.2. Adsorption kinetic models

In order to determine the kinetic mechanism of MB adsorption onto EFB-AC and EFB-UAC, different kinetic models namely; pseudo first order (Cheng et al., 2017; Ho and McKay, 1998), pseudo-second order (Ho and McKay, 1999; Lima et al., 2019), intraparticle diffusion (Ait Ahsaaine et al., 2018) and Elovich kinetic model (Bankole et al., 2019) were utilized to fit the experimental data and these includes:

The pseudo first order model is expressed mathematically as:

$$\text{In}\,(q_e - q_t) = \text{In}\,q_e - k_1 t \tag{13}$$

The pseudo-second-order model is shown as follows:

$$\frac{t}{q_t} = \frac{1}{k_2 q_e^2} + \frac{t}{q_e} \tag{14}$$

The intraparticle diffusion model is expressed by the following equation:

$$q_t = k_{int}t^{1/2} + C \tag{15}$$

The Elovich kinetic model is presented as follows:

$$q_t = \frac{1}{\beta}\text{In}\,(\alpha\beta) + \frac{1}{\beta}\text{In}\,t \tag{16}$$

where q_e (mg/g) = adsorbed amounts of MB at equilibrium, q_t (mg/g) = adsorbed amounts of MB at time t (min), k_1 (min^{-1}), k_2 (mg/g min), k_{int} (mg/g $min^{0.5}$) and α (mg/g min) = pseudo-first order, pseudo-second order, intraparticle diffusion and Elovich rate constants. C (mg/g) = constant for the boundary layer thickness, while β (mg/g min) = constant for the desorption rate relative to the activation energy for chemisorption and extent of surface coverage.

2.8.3. Adsorption thermodynamics

The thermodynamics studies of MB adsorption onto EFB-AC and EFB-UAC were performed to understand the energy changes at various temperatures of 25, 30, 35, 40, 45 and 50 °C. The thermodynamic parameters determined were enthalpy change (ΔH°), Gibbs free energy change (ΔG°) and entropy

change (ΔS°). The Gibbs energy change (ΔG, kJ/mol) of the MB adsorption process was determined by Eq. (17)

$$\Delta G_{ads} = \Delta G^{\circ} + RTInQ \quad (17)$$

where Q describes the quotient of reaction which relates to the MB concentrations of a system that is not in equilibrium. However, at equilibrium $\Delta G_{ads} = 0$. Hence Eq. (17) is reduced to Eq. (18).

$$\Delta G^{\circ} = -RTInk_d \quad (18)$$

where k_d is the equilibrium parameter that can be represented by Eq. (19):

$$k_d = {}^{q_e}\!/_{C_e} \quad (19)$$

where q_e and C_e are the quantity of MB adsorbed at equilibrium and the equilibrium concentration of MB in the solution.

Substituting, $\Delta G^{\circ} = \Delta H^{\circ} - T\Delta S^{\circ}$ into Eq. (17) and dividing by RT, gives:

$$In\, k_d = -\frac{\Delta G^{\circ}}{RT} = \frac{\Delta S^{\circ}}{R} - \frac{\Delta H^{\circ}}{RT} \quad (20)$$

The ΔH° and ΔS° values can be obtained from the slope and intercept of linear regression analysis of the Van't Hoff plots of In k_d against 1/T (Mechi et al., 2019).

2.8.4. Error analysis

All the figures obtained from each experiment and analysis was duplicated. The constants of the isotherm and kinetics studies were determined using Microsoft Excel 2016 software at 95% confidence level. To determine the isotherm and kinetic model fitness to the experimental data in this work, the linear determination coefficient (R^2), the non-linear Chi-square test (χ^2) and the sum of square error (SSE) statistical error analysis tests were carried out. The mathematical equations are represented as follows:

$$X^2 = \sum (q_{e,\,exp} - q_{e,\,cal})^2 / q_{e,\,cal} \quad (21)$$

$$SSE = \sum (q_{e,\,exp} - q_{e,\,cal})^2 \quad (22)$$

where $q_{e,\,exp}$ (mg/g) and $q_{e,\,cal}$ (mg/g) represent the obtained equilibrium capacity from the experimental and model data calculations of the equilibrium capacity respectively. With the small values of χ^2 and SSE, the model data showed similarity to the experimental data. However, if the model data differs with the experimental data, χ^2 and SSE will have higher values. Therefore, it is important to apply χ^2 and SSE to analyze the data and determine the isotherm and kinetic model with the best fit isotherm for the MB adsorption on the adsorbents.

3. Results and discussion

3.1. Characterization of EFB

The results of the proximate and ultimate analysis of EFB revealed that 14.70% moisture content was obtained. Specifically, the volatile matter content of 64.20 wt% indicates that the material is rich in organic matter, and may be suitable for biochar production. The low ash content (3.00 wt%) suggests that the feedstock is good for biochar production. The fixed carbon composition of 18.10 wt% signifies the potential to be transformed into carbonaceous materials during pyrolysis (Liew et al., 2017). In addition, the elemental composition of the EFB showed that the biomass can be converted to biochar residue through pyrolysis. The high carbon content of 44.50 wt% indicates its potential as a feedstock to produce abundant carbon-rich biochar (Liew et al., 2017). The high oxygen content (42.87 wt%) contributes to the surface hydrophobicity and polar nature of the biochar.

The thermal stability of the biomass material presented in Fig. 2a, indicates that the decomposition occurred in two stages. The first stage signifies the removal of moisture while the second stage correspond to the removal of volatile matter present in the EFB (Ma et al., 2017).

The weight loss of about 12% in the temperature range of 100–350 °C, was ascribed to the loss of moisture while in the temperature range 350–500 °C, a weight loss of 62% occurred due to de-volatilization and decomposition of lignocellulose materials (such as hemicellulose, cellulose and lignin).

3.2. Optimization of EFB pyrolysis

The effect of pyrolysis temperature and time on the conversion of EFB to biochar is presented in Table 2. It was observed that the yield of biochar decreased as the temperature increased from 300 °C to 500 °C. Similar trend was noticed for an increase in time. This implied that increase in temperature and time had a negative effect on the yield of biochar.

High yield of 60% and 55% at pyrolysis time of 30 and 60 min were obtained at 300 °C. This high yield of biochar under the applied conditions may be attributed to the reduction of condensation of aliphatic compounds and low emission of CH_4, H_2 and CO. While the decrease in biochar yield may be due to the dehydration effect of hydroxyl groups and thermal degradation of organic compounds (Khalil et al., 2017). More so, the low yield of biochar despite increase in temperature was attributed to biochar formation and availability of liquid and gaseous products.

These results suggest that pyrolysis temperature and time are linearly proportional and as such responsible for the evolution of volatile matter to produce high value biochar needed for activated carbon.

According to Table 2, it was found that the increase in pyrolysis temperature and time caused the shrinkage of material and release of volatile matter. This may be responsible for the observed increase in ash content at 300 °C from 5.00 wt% (30 min) to 11.80 wt% (60 min) and an increase at 500 °C from 5.70 wt% (30 min) to 12.60 wt% (60 min). The ash content suggests the presence of mineral constituents such as K, Na, Al, Fe, Mn and Ca in the sample. These elements could act as inorganic catalysts and improve the pyrolysis process for the production of biochar of a low volatile composition and fixed carbon of higher purity (Liew et al., 2017).

The fixed carbon content of EFB biochar increases with increasing reaction time and temperature. This shows that an increase in temperature and time were directly proportional and exhibited a positive effect on the fixed carbon content. This increment may be ascribed to thermal decomposition of the extractives, tars and hydroxyl acid groups excluding hydrogen and oxygen components (Ma et al., 2017). The biochar from EFB with the highest percentage fixed carbon of 60.40% at 500 °C after 60 min was used for preparation of the activated carbon (EFB-AC and EFB-UAC).

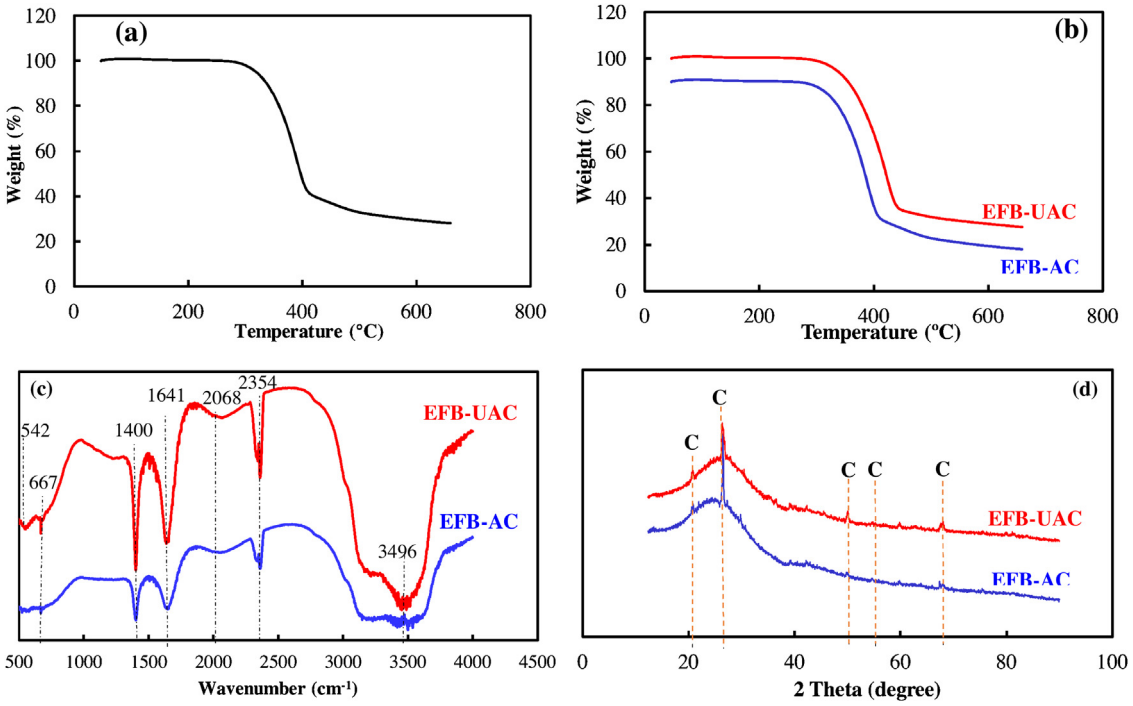

Fig. 2 – Thermogravimetric analysis of (a) EFB; (b) EFB-AC and EFB-UAC at a heating rate of 10 °C/min in a nitrogen environment; (c) FTIR and (d) XRD pattern of EFB-AC and EFB-UAC.

3.3. *Optimization of ultrasonic assisted chemical activation of EFB biochar*

3.3.1. *Effect of activation temperature*

The result of the surface area of the activated carbon developed at different temperatures is presented in Table 3. It can be noticed that at the activation temperatures of 432, 500 and 600 °C, the surface area of EFB-UAC was 1617, 1710 and 2114 m^2/g respectively. In addition, the surface areas of 1591 and 1609 m^2/g were also obtained with further increase in temperature from 700 to 768 °C. Table 3 indicates that the maximum surface area of 2114 m^2/g was obtained under the following process conditions of activation temperature (600 °C), activation time (45 min) and KOH concentration (1.5 M), respectively.

The increment in temperature through sonication assisted activation process contributed to the formation of new pores and enhancement of the existing pores, thereby resulting in increased surface area. Similarly, it was observed that surface area increased over the temperature range of 432–600 °C. On the contrary, further increase in activation temperature beyond 600 °C resulted to decrease in the surface area of the EFB-UAC and was linked to the burn off and destruction of pores at higher temperatures. Altıntıg et al. (2017) had earlier reported surface areas of 940.13 m^2/g for activated carbon upon the increment in activation temperature. In another study, the surface area of 1800 m^2/g was obtained at the activation temperatures of 600 °C (Khalil et al., 2017).

3.3.2. *Effect of activation time*

Table 3 show the result of the effect of sonication enhanced activation time on the surface area of EFB-UAC. According to Table 3, it was observed that the increase in activation time corresponds to increase in the surface area until activation time of 45 min. Beyond the activation time of 45 min, the surface area of EFB-UAC reduced. The surface area of 1470, 1514 and 2114 m^2/g were obtained at the activation time of 20, 30 and 45 min, respectively. On the other hand, further increase in the activation time to 60 and 70 min resulted to decrease in surface area to 1710 and 1650 m^2/g respectively. Therefore, the maximum surface area of 2114 m^2/g was obtained at the activation time of 30 min under the following conditions; constant activation temperature and KOH concentration of 600 °C and 1.5 M, respectively. The results show that activation time has a significant effect on the surface area of the activated carbon under sonication influence.

At low activation time, the surface area was small due to insufficient time for the interaction between activation temperature, KOH concentration and the EFB biochar (Li et al., 2017a,b). However, the reduction in the surface area at higher activation time from 2114 to 1650 m^2/g was attributable to the burn off of pores, widening of the micropores and mesopores or collapse of the pores. Additionally, the reduction in surface area at longer activation time was linked to the liberation of the tar and volatile matter from the carbon surface, accompanied with increased mass loss of the carbon precursor (Li et al., 2017a,b).

3.3.3. *Effect of KOH concentration*

The sonication assisted effect of KOH concentration on the surface area of EFB-UAC was carried out and the result is presented in Table 3. It was noticed that the surface areas of 1569, 1710 and 2114 m^2/g were obtained when KOH concentrations of 0.66, 1.0 and 1.5 M were used for EFB activation. It was further noticed that as the KOH concentration was increased to 2 and 2.34 M, the surface area reduced to 1521 and 1427 m^2/g respectively. Thus, the optimum surface area of 2114 m^2/g was obtained at the activation temperature and time of 600 °C and 45 min respectively.

The KOH concentration plays prominent role on the activation of carbon with the metal intercalate in the carbon lattice act as electron donor which caused the reaction during activation. While oxygen in the alkali removed the carbon atoms cross-linking in the crystallites (Lima et al., 2019). At

Table 3 – Detailed experimental data for the ultrasonic enhanced optimization of the surface area.

Run	Temperature (°C)	Time (min)	KOH concentration (M)	Surface area (m^2/g)
1(FC)	500	60	2	1485
2(FC)	500	30	1	1500
3(FC)	500	30	2	1403
4(FC)	500	60	1	1710
5(FC)	700	30	1	1459
6(FC)	700	60	2	1521
7(FC)	700	60	1	1591
8(FC)	700	30	2	1514
9(AP)	431.82	45	1.5	1617
10(AP)	768.18	45	1.5	1609
11(AP)	600	19.77	1.5	1470
12(AP)	600	70.23	1.5	1650
13(AP)	600	45	0.66	1569
14(AP)	600	45	2.34	1427
15(CP)	600	45	1.5	2113
16(CP)	600	45	1.5	2113
17(CP)	600	45	1.5	2114
18(CP)	600	45	1.5	2113
19(CP)	600	45	1.5	2113
20(CP)	600	45	1.5	2113

FC = Factorial, AP = Axial Point and CP = Center Point.

high KOH concentration, the pore development was prominent and mostly attributed to the intercalation of potassium metal in the carbon structure. The increase in the KOH concentration was responsible for the catalytic oxidation resulting to the formation of new pores and enhancement of the existing ones. This invariably contributed to the increase in the surface area of the EFB-UAC. The activation of EFB biochar with KOH induced porosity network (microporous and mesoporous structure) according to the chemical reactions in Eq. (23) and (24). These reactions alongside liberated carbon dioxide, hydrogen gas and potassium (Lima et al., 2019). Although, the first reaction was more predominant, but both reactions occurred during the activation process.

$$6\,KOH + 2\,C \rightarrow 2\,K + 3\,H_2 + 2\,K_2CO_3 \quad (23)$$

$$KOH + C \rightarrow K + CO + \frac{1}{2}H_2 \quad (24)$$

Thus, EFB-UAC with the specific surface area of 2114 m^2/g was produced under the following conditions; activation time (45 min), activation temperature (600 °C) and KOH concentration (1.5 M)

3.3.4. *Statistical analysis of variance (ANOVA) for ultrasonic assisted production of EFB-UAC*

Central Component Design (CCD) was used to analyze the interaction between the activation temperature, time and concentration of KOH on the surface area under the influence of sonication. The analysis of variance model result for the surface area of developed EFB-UAC is shown in Table 4. According to Table 4, the F-value of 3.477 suggests that the model is significant due to the fact that the p-values is less than 0.0500 (Schüler et al., 2018),

Based on the p-values results in Table 4, activation temperature, activation time and KOH concentration exerted significant effect on the surface area of EFB-UAC. Among the investigated factors, activation time (B) exhibited the greatest effect on the surface area of EFB-UAC with the highest F-value of 82,489.93, followed by KOH concentration (C) with F-value of 50,804.51 and activation temperature (A) with F-value of 107.23. Additionally, the interaction between the activation temperature and KOH concentration (AC) influenced the surface area with the highest F-value of 24,653.26, while activation time and KOH concentration (BC) followed with the F-value of 16,743.21. However, activation temperature and activation time exhibited slight effect on the surface area of EFB-UAC with F-values of 6,123.23. In addition, the value of quadratic function of activation time was the highest on the surface area of EFB-UAC with F-value of 9.439, followed by KOH concentration with the F-value of 1.428 and activation temperature with the F-value of 1.154. This implies that the proposed model fit the experimental data and that the independent variables have considerable effects on the surface area of EFB-UAC activated carbon. The final equation in the term of actual value is given in Eq. (25) as

$$\begin{aligned} \text{Surfacearea} = {} & 2113.18 - 1.94A + 53.73B - 42.16C - 19.12AB \\ & + 38.38AC - 31.62BC - 176.92A^2 - 195.66B^2 - 217.58C^2 \end{aligned} \quad (25)$$

The developed model (Eq. 25) defines the relationship between the activation process parameters and the surface area of activated carbon under sonication influence.

The 3-D surface plots of interaction between the parameters are shown in Fig. 3(a–c). Fig. 3(a) revealed the synergetic effect of activation temperature and activation time on the surface area of activated carbon (EFB-UAC) (at a fixed KOH concentration of 1.5 M), while Fig. 3(b) illustrates the interactive effect of activation temperature and KOH concentration on the surface area of EFB-UAC (at a fixed activation time of 45 min). Also, Fig. 3(c) shows the interactive effect of activation time and KOH concentration on the surface area of activated carbon (at a temperature of 600 °C).

As shown in Fig. 3(a) and (c), at lower activation times, the surface area was not significantly affected by the increase in the activation temperature and KOH concentration due to insufficient time for the carbon to react (Nasrullah et al., 2019). Conversely, at higher activation time shown in Fig. 3(a), it was noticed that the surface area decreased as the activation temperature increased further due to the pores burn off and

Table 4 – ANOVA of response surface model for the surface area of EFB-UAC.

Parameter	Sum of squares	DF	Coefficient estimate	Standard error	F value	P-value	Remark
Model	1.496	9	2113.18	0.28	3.477	<0.0001	Significant
A	51.24	1	−1.94	0.19	107.23	<0.0001	”
B	39419.69	1	53.73	0.19	82,489.93	<0.0001	”
C	24278.10	1	−42.16	0.19	50,804.51	<0.0001	”
AB	2926.13	1	−19.12	0.24	6,123.23	<0.0001	”
AC	11781.13	1	38.38	0.24	24,653.26	<0.0001	”
BC	8001.12	1	−31.62	0.24	16,743.21	<0.0001	”
A^2	4.511	1	−176.92	0.18	9.439	<0.0001	”
B^2	5.517	1	−195.66	0.18	1.154	<0.0001	”
C^2	6.822	1	−217.58	0.18	1.428	<0.0001	”
Lack of fit	3.95				4.73	0.0565	Not significant

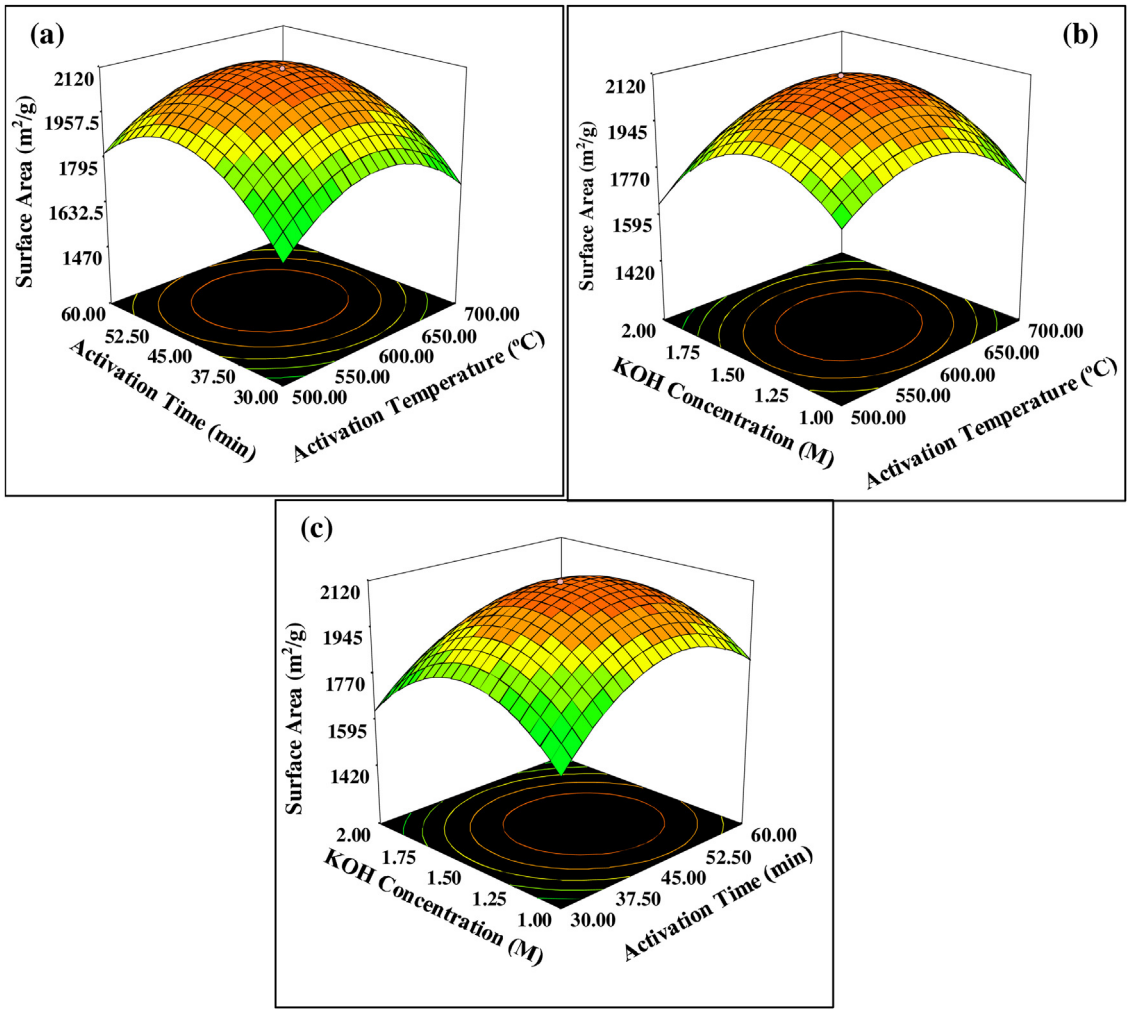

Fig. 3 – The Three-dimensional response surfaces: (a) effect of activation time and temperature (at a fixed KOH concentration of 1.5 M), (b) effect of KOH concentration and activation temperature (at a fixed activation time of 45 min) and (c) effect of KOH concentration and time (at a fixed temperature of 600 °C) on the surface area of EFB-UAC.

widening of micropores and mesopores (Khalil et al., 2017). Not only that, tar and volatile matter were liberated from the surface of carbon at high activation temperature and high activation time, which further increased the weight loss of the carbon precursor. It is obvious from Fig. 3(b) that there was a strong interaction between the activation temperature and KOH concentration with F value of 24,653.26 on the surface area of EFB-UAC. The increase in surface area with increasing impregnation ratio to the optimum point of 2114 m^2/g was due to the continuous evolution of volatile products under the influence of ultrasonication. The sonication phenomenon enhanced the dehydration and elimination process (Nasrullah et al., 2019). Similarly, further addition of KOH resulted to decrease in surface area due to the hindrance of tars and liquids formation which blocked the pores on the carbon surface during activation (see Fig. 3(b)).

3.4. *Characterization of EFB-AC and EFB-UAC*

3.4.1. *BET surface area of EFB-AC and EFB-UAC*

The surface area of the pyrolyzed biochar and developed activated carbon was analyzed using BET and the results revealed that the EFB-AC had a surface area of 1036 m^2/g with the corresponding pore volume and pore size of 0.052 m^3/g and

6.84 nm respectively. However, the surface area of the EFB-UAC (2114 m^2/g) with the pore volume of 0.26 m^3/g and pore size of 4.35 nm almost doubled that of EFB-AC. The significant improvement in the surface area of EFB-UAC was linked to the sonication effects which open the micro and macropores of the material. The result of the surface area obtained in this study was thrice the surface area of 828.3 m^2/g reported by Islam et al. (2017). The differences in the results could be linked to the ultrasonic effect employed in this current study and also the strong interactive effects among the parameters such as the activation time, activation temperature and the activating agent utilized.

3.4.2. TGA of EFB-AC and EFB-UAC

Fig. 2(b) shows the result of the thermal profiles of the prepared EFB-AC and EFB-UAC. Two decomposition stages were observed. Notably, for EFB-AC, a weight loss of about 1.96 wt% was observed, and was attributed to evaporation of moisture adsorbed on the sample between the temperatures of 100 °C to 300 °C. Furthermore, a weight loss of the EFB-AC increased to 74.15 wt% as the temperature increased from 300 °C to 500 °C. This significant weight loss was due to depolymerization, graphitization and volatilization of the EFB-AC. Also, 21.37 wt% weight loss was observed beyond 500 °C attributable to the loss of the residual inorganic and organic compounds. Also in Fig. 2(b), the initial weight loss of 1.06%, which occurred in the temperature range of 50 °C to 300 °C and depict the loss of adsorbed moisture.

In the second stage, significant weight loss of 67.74% was noticed in the temperature range of 300 °C to 500 °C. This was linked to the decomposition of volatile constituents. The decompositions of both residual organic compounds and inorganic constituents above 500 °C resulted to corresponding weight loss of 14.44%. Comparatively, it can be concluded that EFB-UAC was more thermally stable than EFB-AC due to the cavitation impact induced by the ultrasonic enhanced activation process on the former than the latter.

3.4.3. FTIR of EFB-AC and EFB-UAC

The functional groups on the EFB-AC and EFB-UAC were examined using FTIR technique and the result presented in Fig. 2(c). The FTIR spectra of the EFB-AC and EFB-UAC show the presence of the following absorption bands at 667, 1400, 1641, 2068, 2354 and 3496 cm^{-1} respectively. Among the adsorption peaks, it was noticed that the intensity of the following bands observed at 1400 cm^{-1}(C—C), 1641 cm^{-1}(C=O) and 2354 cm^{-1}(C≡C) was strong and predominant on the EFB-UAC than on the EFB-AC due to the ultrasonication effect. The low intensity of peaks on the EFB-AC spectra may be due to elimination of oxygenated compounds during activation conversion of biochar into activated carbon (Ma et al., 2017). Similarly, the occurrence of peaks of low intensity may be explained in terms of decomposition of oxygenated compounds accompanied with the released of volatile lignocellulosic components (Liew et al., 2017). Interestingly, the sharp peak on the EFB-UAC that occurred at 542 cm^{-1}(C—H) was conspicuously missing on the EFB-AC and could be linked to the sonication influence of activation on the EFB-UAC. The absorbance peak at 667 cm^{-1} was ascribed to the vibrational bending of C—H and O—H in alkane, alcohol or phenolic groups in the EFB-UAC (Kazak et al., 2017).

Also, the absorption peak at 2068 cm^{-1} suggests the presence of C=O stretch of carbonyl and carboxyl groups. The formation of broad band at the wavelength of 3496 cm^{-1} represents O—H stretching revealing the presence of hydroxyl groups from aliphatic alcohols, phenolic compounds and carboxylic acid (Kazak et al., 2018). It is also evident that the peak depicting hydroxyl group in the EFB-AC spectra was of low intensity compared to the large broad band exhibited by the EFB-UAC. The broad nature of the peaks at wavelength of 3496 cm^{-1} for the EFB-UAC may be due to the cavitation influence.

3.4.4. XRD of EFB-AC and EFB-UAC

Fig. 2(d) shows the XRD pattern of the produced EFB-AC and the EFB-UAC. There were presence of five peaks at 2θ values of 20.60°, 26.33°, 50.93°, 59.88° and 68.00° which corresponds to the following crystal planes (111), (002), (102), (202) and (220). The identified peaks and crystal planes on the EFB-AC and EFB-UAC confirmed the formation of crystalline carbon. However, it was observed that the peak at 26.33° (002) was sharper and more intense than other four peaks on both the EFB-AC and the EFB-UAC. The peak identified at 26.33° showed similarity with the peak reported by Ma et al. (2017) in their work. The sharp and intense peaks observed on the EFB-UAC compared to the smaller peaks on the EFB-AC could be attributed to the active effect of KOH through ultrasonic assisted activation process.

The crystallite sizes of the EFB-AC and the EFB-UAC calculated using Debyne–Scherrer equation expressed as follows;

$$D = \frac{K\lambda}{\beta\cos\theta} \tag{26}$$

where D (nm) is the mean crystallite sizes, K denotes the crystallite shape factor called Scherrer constant with value between 0.2 and 2.0 (0.94 for cubic structures), λ (nm) refers to the X-ray wavelength (0.154 nm), β (radians) is the full width at half maximum (FWHM) of the diffraction peak in the XRD pattern and θ (deg) is the diffraction angle calculated from the 2θ values of the XRD pattern. The evaluated crystallite sizes ranged from 44 to 120 nm and 6 to 60 nm respectively. The average crystallite size of 64 and 28 nm obtained, suggested the polycrystalline nature of the EFB-AC and the EFB-UAC. The small crystallite sizes obtained for the EFB-UAC could also be linked to the significant influence of sonication during chemical activation of EFB biochar by KOH.

3.4.5. HRSEM-EDS of EFB-AC and EFB-UAC

The surface morphology of the EFB-AC and the EFB-UAC was examined using HRSEM and the micrograph is presented in Fig. 4(a) and (b). As shown in Fig. 4(a) and (b), distinguishable structural network were identified on the EFB-AC and the EFB-UAC and could be linked to the applied preparation conditions. Not only that, pyrolysis temperatures resulted in the decomposition of EFB causing evolution of volatile substances to form new pores in EFB-AC (Fig. 4a). However, these pores were enhanced and new pores formed during the sonication assisted activation process as shown by the arrows in Fig. 4(b). The HRSEM of the EFB-AC shows that the surface contains fewer cavities, while the surface of the EFB-UAC revealed numerous cavities of different sizes and shapes. Therefore, the surface of the EFB-UAC was more porous in nature than the EFB-AC due to the presence of cell pores and cavities of different diameter.

The pores formation after activation was attributed to the escape of some volatiles organic constituents as well as KOH activating agent from the sample (Kazak et al., 2017).

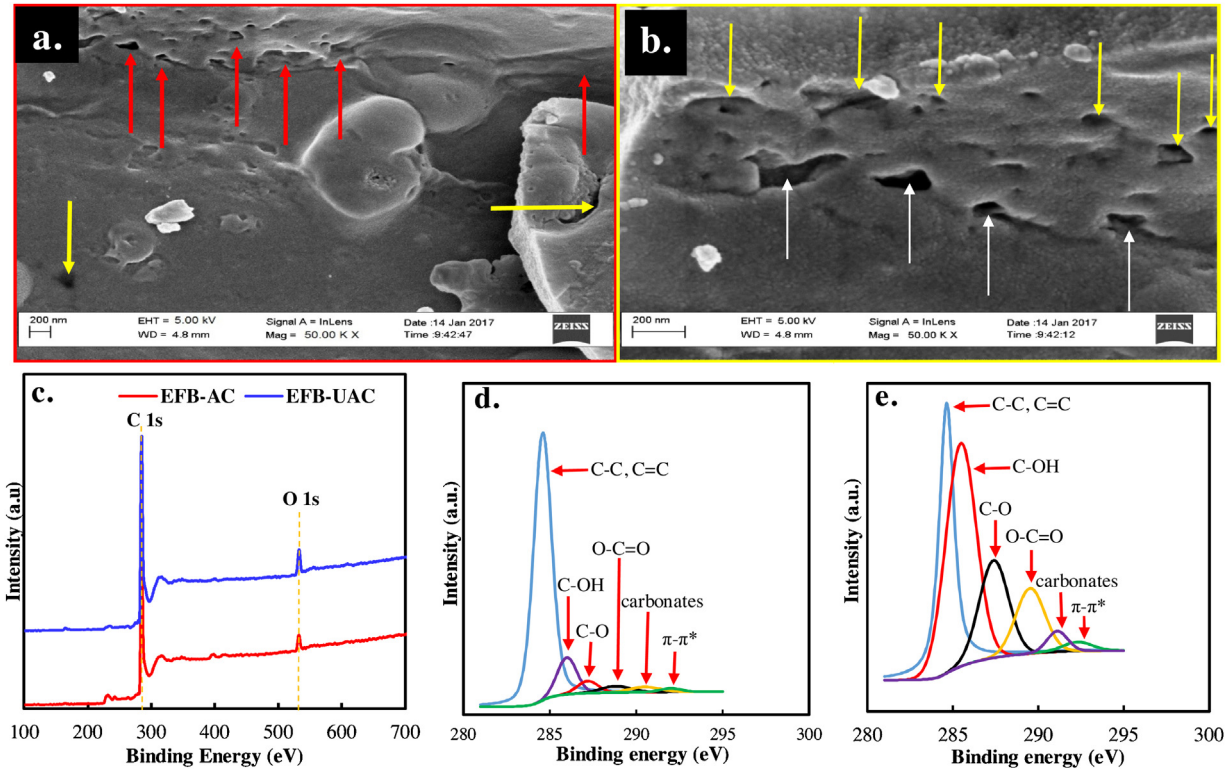

Fig. 4 – HRSEM of (a) EFB-AC; (b) EFB-UAC; (c) XPS spectra and High-resolution C 1s XPS spectra of (d) EFB-AC and (e) EFB-UAC.

The elemental composition of the EFB-AC and the ultrasonic enhanced EFB-UAC revealed element carbon as the fundamental component of the material with 76.37% and 81.81% respectively. It was also observed that oxygen ranked second with 21.80% and 16.60% on the EFB-AC and EFB-UAC. Although there was a negligible amount of Si (0.72 and 0.55%) on the EFB-AC and the EFB-UAC, while the calcium contents were identified to be 1.11% and 0.70%. However, the presence of potassium (0.34%) was identified on the EFB-UAC which could be due to the KOH used for the activation.

3.4.6. *XPS of EFB-AC and EFB-UAC*

The oxidation states of the elements present on the surface of the EFB-AC and the EFB-UAC along with their functional groups were determined using XPS method. The elements identified on the surface of the EFB-AC and the EFB-UAC through XPS measurements were predominantly C (1s) and O (1s) as shown in Fig. 4(c). The binding energies region for the C (1s) and oxygen O (1s) were 286.6 eV and 534 eV respectively. The XPS analysis revealed an increase in the carbon and oxygen content on the surface of EFB-AC and EFB-UAC adsorbents. However, the oxygen content on the surface of EFB-UAC was higher than EFB-AC surface. The improved oxygen content on EFB-UAC may be due to the ultrasonic enhanced activation of the adsorbent (Kazak et al., 2018).

In addition, a high-resolution C (1s) spectra fitted to the deconvolution peaks for carbon and the identified functional groups on the adsorbents surface are illustrated in Fig. 4(d) and (e). As shown in Fig. 4(d) and (e), the main element is C with peaks occurrence at the binding energy of 284.6 eV (C 1s)). The binding energy of C (1s) in the XPS spectrum deconvoluted at 284.6 eV confirmed the presence of the functional groups (C—C, C=C). While other binding energies at 286.1, 287.3, 288.9 eV belong to the functional groups (C—OH), (C=O) and (O—C=O) found on the surface of EFB-AC adsorbent. Similarly, the deconvoluted peaks and the surface functional groups on the EFB-UAC were observed at 284.8 (C—C, C=C), 287.8 (C—OH), 289.5 (C=O) and 290.8 eV (O—C=O). This study shows that the EFB-UAC has more C—C (graphite) bonds compared to EFB-AC. This may be due to ultrasonic influence on the activation process. The transitional loss of peaks which connote the chemical force of attraction on the surface of the EFB-AC and the EFB-UAC is denoted by π–π^*. The functional groups obtained in XPS analysis were consistent with the results of FTIR analysis in Fig. 2(c).

3.5. *Ultrasonic assisted adsorption experimental result*

3.5.1. *Ultrasonic enhanced effect of adsorbent dosage on MB adsorption*

Adsorbent dosage is ranked as a major parameter promoting adsorption process because it anchors the binding sites on surface on the adsorbent (Bankole et al., 2019). The ultrasonic enhanced effect of adsorbent dosage on the MB adsorption by EFB-AC and EFB-UAC was evaluated in the range 10–60 mg. According to Fig. 5(a) and (b), it was found that as the weight of EFB-AC and EFB-UAC was increased from 10 mg to 60 mg, the adsorption capacity equally increased from 70.8 to 290 mg/g and 75 to 307 mg/g respectively. The increased adsorption of MB at higher dosage was linked to the increase in the number of binding sites and bulk surface area (Miyah et al., 2018). In addition, it was observed that as the adsorbent dosage was adjusted above 30 mg, the uptake of MB by EFB-AC and EFB-UAC was not rapid due to possible aggregation, thus limiting the active surfaces for adsorption (Khalil et al., 2017). The optimum dosage obtained for MB removal in this study was 30 mg of the adsorbents. Comparatively, it was noticed that EFB-UAC adsorbed more MB molecules at the various adsorbent dosage than EFB-AC. This could be attributed to ultrasonic effect and

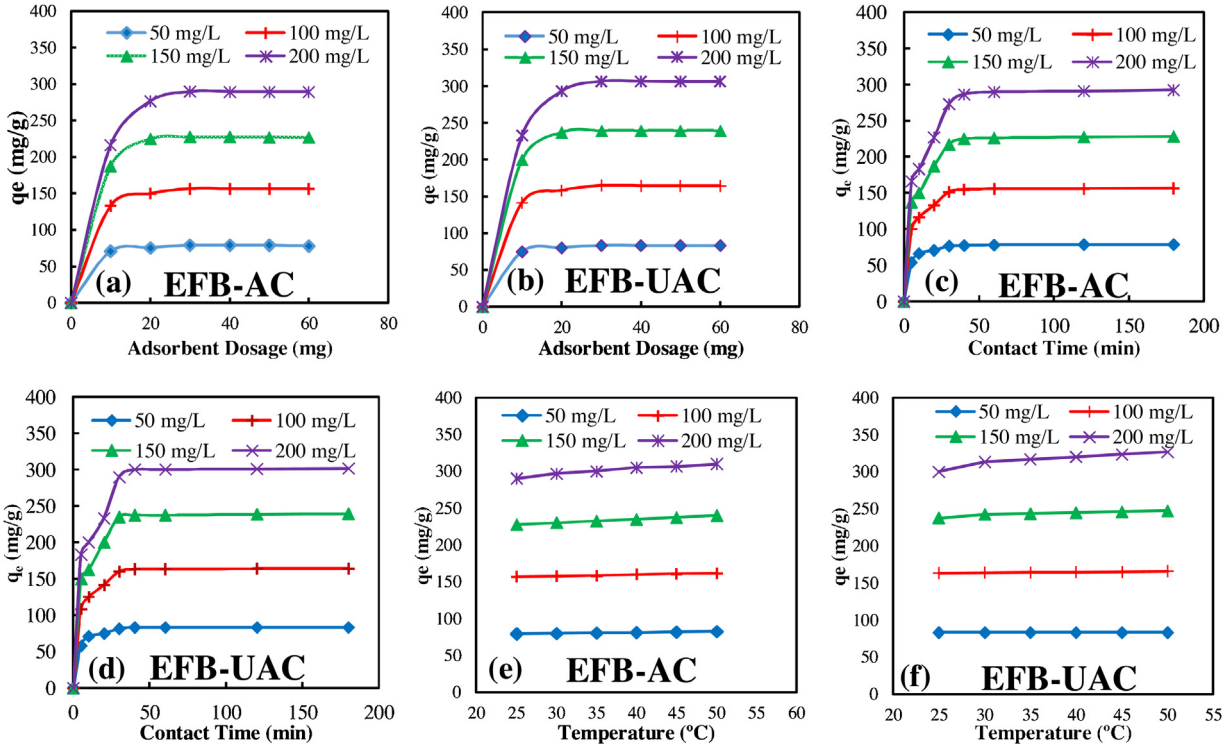

Fig. 5 – Effect of adsorbent dose on the MB adsorption onto (a) EFB-AC and (b) EFB-UAC (at contact time = 20 min, temp. = 30 °C and pH = 6), effect of contact time on the MB adsorption onto (c) EFB-AC and (d) EFB-UAC (at adsorbent dosage = 30 mg, temp. = 30 °C and pH = 6) and effect of solution temperature on the MB adsorption onto (e) EFB-AC and (f) EFB-UAC(at adsorbent dosage = 30 mg, contact time = 40 min and pH = 6).

the enhanced surface area, pores formation and surface functional groups of the EFB-UAC relative to EFB-AC.

3.5.2. *Ultrasonic enhanced effect of contact time on MB adsorption*

The results of effect of contact time on the MB adsorption using EFB-AC and EFB-UAC are presented in Fig. 5(c) and (d). It was observed that rapid adsorption occurred in the first 30 min of the sonication time at the various initial MB concentration of 50, 100, 150 and 200 mg/L which was linked to the external diffusion of MB molecules to the enormous number of the adsorption sites available at this time region (Mouni et al., 2018). Also, the adsorption of MB molecules onto EFB-AC and EFB-UAC gradually increased beyond 30 min and could be attributed to the influence of intraparticle diffusion (Kazak et al., 2018). As shown in Fig. 5(c) and (d), the adsorption equilibrium was attained in 40 min at the various MB concentrations and negligible increase in the MB adsorption was noticed at longer sonication times. In addition, two adsorption stages (rapid and equilibrium) were identified. The rapid adsorption stage illustrates strong electrostatic attractions between MB solution and the surface of activated carbon, while the insignificant adsorption of MB at equilibrium (stable) stage indicates the saturation of active sites on the surface of activated carbon (Ait Ahsaaine et al., 2018). Furthermore, the amount of MB adsorbed increased from 54.16 to 58.33 mg/g and 292.66 to 301.67 mg/g using EFB-AC and EFB-UAC respectively. At every contact time, it was observed that EFB-UAC sequestered more of the MB molecules from aqueous solution than EFB-AC. This was ascribed to the enhanced ultrasonic effect and higher surface area and presence of more functional groups on EFB-UAC than EFB-AC.

3.5.3. *Ultrasonic enhanced effect of temperature on MB adsorption*

Temperature is an important parameter in adsorption process and was investigated in the range of 25–50 °C for different initial MB concentrations (50, 100, 150 and 200 mg/L). As presented in Fig. 5(e) and (f), it was revealed that the effect of temperature on MB adsorption was low at MB concentrations of 50 and 100 mg/L, but however increased at higher concentrations of 150 and 200 mg/L. This may be attributable to increased scattering rate of MB molecules across the internal pores of adsorbent particles with increase in temperature. Fig. 5(e) and (f) indicates that temperature is a significant parameter in adsorption process due to the increase in MB adsorbed quantity in the studied temperature range. In addition, increase in temperature translated to increase in the adsorption capacity of MB adsorption at different MB concentrations, indicating that the adsorption process is kinetically controlled. It was observed that the adsorption capacities increased from 79.16–310 mg/g and 83.33–326.67 mg/g for MB adsorption onto EPB-AC and EFB-UAC, respectively. The MB adsorption onto EFB-AC and EFB-UAC was endothermic in nature, indicating a favorable adsorption process. This behavior could be due to decrease in the solution viscosity that favors external transfer and adsorbate (MB) diffusion within the solid adsorbent (EFB-AC and EFB-UAC) (Miyah et al., 2018). The increased MB adsorption with increase in temperature could be linked to: (1) the increase in MB mobility, thereby enabling its penetration to the pores of the adsorbent; (2) the increased chemical interactions of the MB with the functional groups on the surface of EFB-AC and EFB-UAC; and (3) the chemical potential change, associated with the solubility of MB species (Lima et al., 2019).

3.5.4. *Ultrasonic enhanced effect of pH on MB adsorption*

The pH of solution controls both the adsorbent surface chemistry and the solubility of MB (Lu et al., 2019). The ultrasonic enhanced influence of solution pH on MB adsorption onto EFB-AC and EFB-UAC was investigated. As shown in Fig. 6(a), the MB/EFB-AC and MB/EFB-UAC systems were impacted by the solution pH. The MB adsorption increased as the solution pH was increased from 2 to 10 and the adsorption capacities increased from 305 to 455 mg/g and 330 to 495 mg/g for MB adsorption onto EFB-AC and EFB-UAC respectively. The increased removal of MB at high pH may be ascribed to the fact that the EFB-AC and EFB-UAC became negatively charged and easily adsorbed positively charged MB via electrostatic attraction (Wang et al., 2018c).

As shown in Fig. 6(b) and (c), the adsorbents point of zero charge (pH_{PZC}) were estimated to be 6.5 and 6.6 respectively. This indicates that the EFB-AC and EFB-UAC adsorbent surface may be positively charged at pH < 6.5 and 6.6, respectively. Consequently, a strong electrostatic repulsion could occur between MB and the positively charged EFB-AC and EFB-UAC, thus inhibiting MB adsorption by the two materials. Also, competitive adsorption was observed between MB and excess H^+ in acidic pH. On the contrary, the surface of EFB-AC and EFB-UAC became negatively charged at pH > 6.5 and 6.6 respectively and thus, weakened the electrostatic repulsive force and enhanced the adsorption of MB on the surface of EFB-AC and EFB-UAC (Ait Ahsaaine et al., 2018). The results obtained shows that pH adjustment of wastewater is very important to achieve improved adsorption of MB by EFB-AC and EFB-UAC.

3.5.5. *Ultrasonic enhanced effect of initial MB concentration on the adsorption process*

The influence of initial MB concentration on MB adsorption by EFB-AC and EFB-UAC was studied and the result is presented in Fig. 6(d). According to Fig. 6(d), the MB adsorption onto the EFB-AC and EFB-UAC increased as the initial MB concentration was increased. The adsorption capacity of MB adsorption onto EFB-AC and EFB-UAC was observed to increase from 79.16 to 290 mg/g and 83.33 to 306.67 mg/g, respectively. The increasing trend of MB adsorbed amount could be due to ease of contact between the active sites of the EFB-AC and EFB-UAC and the MB molecules. In addition, the driving force provided by the initial MB concentration overcame the resistance of MB mass transfer. The removal efficiency of MB molecules by the EFB-AC and EFB-UAC adsorbents presented in Fig. 6(e) indicates that removal efficiency of MB decreased as the MB initial concentration was increased. The highest removal efficiency (95% and 100%) was obtained at 50 mg/L using EFB-AC and EFB-UAC respectively. This could be attributed to decrease in binding sites on adsorbent surface and increased repulsive force between the adsorbent surface and MB molecules (Shu et al., 2018).

3.5.6. *Effect of ionic strength on MB adsorption*

Inorganic salts are frequently utilized as additive in dye promoting agents and levelling agents during treatment (Lu et al., 2019). Hence, it is important to investigate the effect of inorganic salts on the adsorption performance of EFB-AC and EFB-UAC. It was observed from the ionic strength result in Fig. 6(f). that increase in the ionic strength decreased MB removal efficiency. At the initial electrolyte of 0.01 mol/L Na^+, 96% and 99% of MB was adsorbed by EFB-AC and EFB-UAC respectively, however as the concentration of the electrolyte increased from 0.1 to 1 mol/L Na^+, the MB adsorbed decreased from 84 to 48% and 90 to 65%. However, 93% and 98% of MB were adsorbed at the initial electrolyte concentration of 0.01 mol/L Ca^{2+} for EFB-AC and EFB-UAC respectively. As the electrolyte concentration increased from 0.1–1 mol/L Ca^{2+}, the MB adsorbed decreased from 70 to 35% and 78 to 40% using EFB-AC and EFB-UAC respectively. The result shows that the addition of Na^+ and Ca^{2+} to the MB solution inhibited MB removal due to stronger competition between salt ions on the surface of adsorbents and cationic MB (Li et al., 2019). Also, it was observed that Ca^{2+} posed higher inhibiting effect than Na^+ at the same concentration due to higher valence state of Ca^{2+} than Na^+. The adsorption of Ca^{2+} on the EFB-AC and EFB-UAC surface produced stronger electrostatic repulsion onto MB adsorption than Na^+.

3.6. *Adsorption isotherms*

The MB dye interaction with the adsorbents (EFB-AC and EFB-UAC) as a function of adsorption parameters were evaluated using adsorption isotherm models namely; Langmuir, Freundlich, Temkin and D–R. This was done to correlate the equilibrium experimental data of MB adsorption by EFB-AC and EFB-UAC. The plots from the four different isotherm models are shown in Figs. S1 and S2, and the calculated parameters are presented in Table 5.

The fitness of each isotherm was evaluated on the basis of R^2, SSE and X^2 and the experimental data was best described by the Langmuir model with high R^2 values (0.998–0.999) compared to Freundlich (0.805–0.998), Temkin (0.815–0.999) and D–R (0.664–0.978). In addition, the lowest values obtained from the error analysis using statistical parameters (X^2 and SSE) equally validated the fitness of the model. Therefore, it can be affirmed that Langmuir isotherm model showed the homogeneous nature of the EFB-AC and EFB-UAC surface and monolayer coverage of the MB molecule. Generally, Langmuir isotherm assumes that: (i) It was not possible for adsorption to advance outside monolayer coverage. (ii) The sites on the surface are equivalent and only accommodate a molecule of the adsorbate. (iii) MB molecules ability to adsorb at a specified site is not dependent on the neighboring sites occupation (Ait Ahsaaine et al., 2018). More so, the determined (R_L) values were between 0.008–0.112 and 0.001–0.055 for both the EFB-AC and EFB-UAC, indicated a favorable adsorption of MB molecules under the applied conditions. The Langmuir maximum adsorption capacity (q_m) which assumes monolayer adsorption for the uptake of MB molecules by EFB-AC and EFB-UAC was equal to 400 and 434 mg/g respectively. Also, the Langmuir model showed close correlation between the calculated q_m and the experimental q_m. This result is considerably better than the previously reported adsorbents in the literature. For instance, an adsorption capacity of 166.51 mg/g have been reported of activated carbon from banana trunk for dye removal (Danish et al., 2018b). In addition, a microporous carbon from cotton waste was reported to have an adsorption capacity of 369.48 mg/g (Tian et al., 2019). The maximum adsorption capacities of MB onto EFB-AC and EFB-UAC in this study and in the literature are summarized in Table 6. According to Table 6, EFB-AC and EFB-UAC were considered favorable alternative for the MB adsorption from liquid media.

3.7. *Adsorption kinetics*

The non-linear pseudo-first order, pseudo-second order, Elovich and intraparticle diffusion models were adapted and

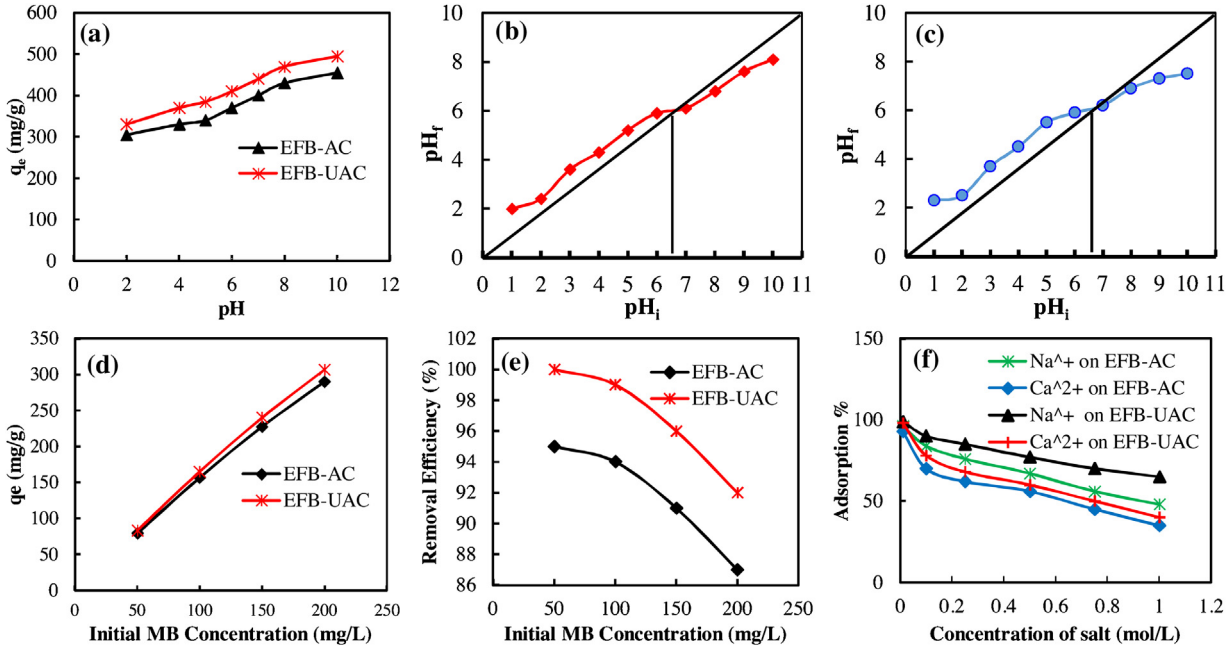

Fig. 6 – (a) Effect of solution pH on MB adsorption capacity of EFB-AC and EFB-UAC (at adsorbent dosage = 30 mg, contact time = 40 min, MB initial conc. = 100 mg/L and temp. = 50 °C); (b) EFB-AC Point of zero charge (pH_{PZC}) determined by pH drift method; (c) EFB-UAC Point of zero charge (pH_{PZC}) determined by pH drift method; (d) effect of initial MB concentration on the adsorption capacity of EFB-AC and EFB-UAC (at adsorbent dosage = 30 mg, contact time = 40 min, pH = 10 and temp = 50 °C); (e) effect of initial MB concentration on the adsorption efficiency by EFB-AC and EFB-UAC (at adsorbent dosage = 30 mg, contact time = 40 min, pH = 10 and temp = 50 °C); (f) effect of ionic strength (NaCa) on the MB removal efficiency by EFB-AC and EFB-UAC (at adsorbent dosage = 30 mg, contact time = 40 min, temp = 50 °C and MB initial conc. = 100 mg/L).

Table 5 – Parameters of isotherm models for MB adsorption onto EFB-AC and EFB-UAC.

Isotherm	Parameters	EFB-AC				EFB-UAC			
		50 mg/L	100 mg/L	150 mg/L	200 mg/L	50 mg/L	100 mg/L	150 mg/L	200 mg/L
Langmuir	q_m (mg/g)	68	167	233	400	77	196	312	434
	K_L (L min^{-1})	2.508	0.600	0.212	0.050	65.000	3.188	0.485	0.097
	R_L	0.008	0.017	0.032	0.112	0.001	0.003	0.014	0.055
	R^2	0.999	0.999	0.999	0.998	0.999	0.999	0.999	0.999
	SSE	0.060	0.008	0.001	0.020	0.055	0.081	0.029	0.020
	X^2	0.012	0.010	0.000	0.072	0.040	0.056	0.062	0.068
Freundlich	N	5.173	4.704	2.757	1.413	4.039	3.342	1.982	1.030
	K_F (mg/g)	86.936	198.335	295.393	757.530	79.763	166.265	295.393	542.750
	R^2	0.978	0.977	0.998	0.988	0.805	0.910	0.994	0.979
	SSE	0.179	0.263	0.304	2.615	1.737	1.599	0.537	3.220
	X^2	0.215	0.203	0.184	0.960	0.392	0.180	0.112	0.102
Temkin	b_T (kJ/mol)	−1847.62	−1448.66	−1038.29	−740.06	−16866	−3433.79	−1635	−996.6
	A_T (L/g)	0.86×10^{-5}	4.0×10^{-5}	22.9×10^{-5}	74.3×10^{-5}	1.4×10^{-6}	8.4×10^{-5}	1.1×10^{-5}	2.3×10^{-4}
	R^2	0.982	0.981	0.999	0.992	0.815	0.919	0.994	0.984
	SSE	0.256	0.183	0.176	0.663	0.631	0.325	0.269	1.705
	X^2	0.131	0.120	0.108	0.214	0.247	0.141	0.102	0.205
D–R	K_{ad}	2×10^{-6}	6×10^{-6}	9×10^{-6}	4×10^{-5}	1×10^{-5}	5×10^{-5}	2×10^{-6}	1×10^{-6}
	q_s	71.215	135.409	182.71	214.198	79.623	149.038	201.361	240.591
	R^2	0.875	0.856	0.978	0.906	0.664	0.691	0.915	0.837
	SSE	3.233	5.887	20.147	57.970	1.768	2.579	14.922	23.654
	X^2	0.888	3.337	10.980	26.826	0.173	1.710	7.414	18.147

fitted to the experimental data obtained and the plots are shown in Figs. S3 and S4. The values of the calculated kinetic parameters obtained for the four kinetic models as well as the R^2, SSE and X^2 are presented in Table 7. According to Table 7, pseudo-second order kinetic model demonstrated better correlation with the experimental data due to a higher (R^2) and a lower SSE and (X^2) error values. Also, a significant agreement of the experimental ($q_{e,exp}$) and the calculated ($q_{e,cal}$) adsorption capacity showed the best fitness of pseudo-second order kinetic model.

Similarly, the initial rates of adsorption (h_0) with higher values were illustrated by pseudo-second order model which indicated the significance of the adsorption at the initial values of contact time. In view of the obtained values in this study, the mechanism of MB adsorption by EFB-AC and EFB-UAC was strongly driven by chemisorption phenomenon, under the influence of the chemical characteristics of the MB and adsorbents (Lima et al., 2019). Furthermore, Elovich kinetic model shown in Table 7 revealed that the values of β were lesser than the values of α, suggesting rapid adsorption mechanism

Table 6 – Comparison of maximum adsorption capacity and BET surface area for EFB-AC and EFB-UAC with various adsorbents described in the literature.

Adsorbent	q_m (mg/g)	Activating agent	S_{BET}	pH	Contact time (min)	Dosage (g/L)	Co (mg/L)	T (^{o}C)	Reference
BTAC	166.51	H_3PO_4	1173	–	20	1.5	250	25	Danish et al. (2018b)
AC-Fe/Zn-0.5-400-1	369.48	$FeCl_3/ZnCl_2$	1342	10.0	1440	0.05	400	25	Tian et al. (2019)
ACZ	386	$ZnCl_2$	1817	–	720	0.1	600	25	Khalil et al. (2017)
Fe-AC	357.1	$ZnCl_2$	940.13	4.0	60	0.05	250	25	Altıntıg et al. (2017)
ABC	53.23	HNO_3	37.5	8.0	720	1.0	50	25	Wang et al. (2018c)
Fe-Ce-AC	264.55	Fe-Ce	776.2	7.0	180	2.0	400	40	Cheng et al. (2018)
AMH1	159.89	$H_3PO_4/ZnCl_2$	1161.3	6.0	60	2.0	329	27	Danish et al. (2018a)
HAC-EA	270	KOH	823	7.0	1440	2.0	700	25	El-Shafey et al. (2016)
Beer solid wastes AC	161	CO_2	80	6.5	120	1.0	500	25	Franciski et al. (2018)
Waste carpets AC	403.2	H_3PO_4	330	8.0	720	8.0	700	35	Hassan and Elhadidy (2017)
KFHAC	239.4	KOH	828.3	7.0	1440	0.2	400	50	Islam et al. (2017)
LSC	210.97	CO_2	733	11.0	120	0.012	10	60	Li et al. (2018)
ACC	149.11	K_2CO_3	355.11	9.0	1560	1.0	400	30	Marrakchi et al. (2017)
Waste cork powder	350	Alkaline waste H_2O	1670	7.0	10	2	700	20	Novais et al. (2018)
PG/C-A450-2/1	351	$ZnCl_2$	1044	7.0	1440	0.4	300	30	Zhang et al. (2015)
PC	320.53	KOH	1187.8	7.9	720	0.1	400	30	Charola et al. (2019)
EFB-AC	400	KOH	40	10.0	40	0.03	200	50	This study
EFB-UAC	435	KOH	40	10.0	40	0.03	200	50	This study

Table 7 – Parameters of four kinetic models for MB adsorption onto EFB-AC and EFB-UAC.

Kinetics	Parameters	EFB-AC				EFB-UAC			
		50 mg/L	100 mg/L	150 mg/L	200 mg/L	50 mg/L	100 mg/L	150 mg/L	200 mg/L
	$q_{e,exp}$ (mg/g)	77.50	153.33	225.00	283.33	83.333	163.333	237.500	300.000
PFO	$q_{e,cal}$ (mg/g)	31.05	108.14	150.11	158.05	98.719	41.486	150.107	181.970
	K_1 (g mg^{-1} min^{-1})	−0.083	−0.107	−0.079	−0.051	−0.093	−0.100	−0.079	−0.063
	R^2	0.969	0.932	0.966	0.994	0.949	0.939	0.966	0.950
	SSE	2157.347	2042.131	5609.010	15695.412	236.714	14846.809	7637.594	13931.061
	X^2	69.474	18.884	37.367	99.305	2.398	357.876	50.881	76.557
PSO	$q_{e,cal}$ (mg/g)	78.06	154.08	225.73	284.09	82.64	163.93	238.10	300.30
	K_2 (g mg^{-1} min^{-1})	0.008	0.003	0.002	0.001	0.013	0.004	0.002	0.001
	h_0 (mg g^{-1} min^{-1})	48.08	68.03	82.64	75.76	86.21	103.09	103.09	90.91
	R^2	1.000	1.000	0.999	0.999	1.000	1.000	0.999	0.999
	SSE	0.318	0.562	0.538	0.574	0.474	0.361	0.354	0.090
	X^2	0.004	0.004	0.002	0.002	0.006	0.002	0.001	0.000
Elovich	α (g mg^{-1} min^{-2})	17657.912	3004.076	1268.532	783.851	4648.932	7619.135	2444.856	1447.050
	β (mg g^{-1} min^{-1})	0.158	0.062	0.037	0.027	0.161	0.066	0.038	0.028
	R^2	0.791	0.817	0.804	0.848	0.719	0.770	0.785	0.818
	SSE	6.091	8.127	10.890	17.052	2.146	5.559	7.242	13.157
	X^2	1.750	2.705	8.584	11.599	1.462	3.296	6.393	9.092
IPD	k_t (g mg^{-1} min^{-1})	1.667	4.265	7.215	10.351	1.576	3.958	6.926	9.894
	C (mg/g)	61.295	111.330	149.930	176.650	66.487	121.100	163.430	194.310
	R^2	0.556	0.588	0.584	0.652	0.471	0.531	0.561	0.619
	SSE	262.602	1764.280	5635.505	11381.334	283.799	1783.654	5486.365	11170.376
	X^2	4.284	15.847	37.588	64.429	4.268	14.729	33.570	57.487

PFO = Pseudo-first order, PSO = Pseudo-second order and IPD = Intraparticle diffusion.

Table 8 – Thermodynamic parameters for MB adsorption onto EFB-AC and EFB-UAC.

	EFB-AC			EFB-UAC		
T (°C)	ΔG^{o} (kJ/mol)	ΔH^{o} (kJ/mol)	ΔS^{o} (J/mol)	ΔG^{o} (kJ/mol)	ΔH^{o} (kJ/mol)	ΔS^{o} (kJ/mol)
25	1141.94	288.09	−34.15	1744.31	480.07	−50.57
30	1312.71			1997.16		
35	1483.48			2250.01		
40	1654.24			2502.86		
45	1825.01			2755.71		
50	1995.78			3008.56		

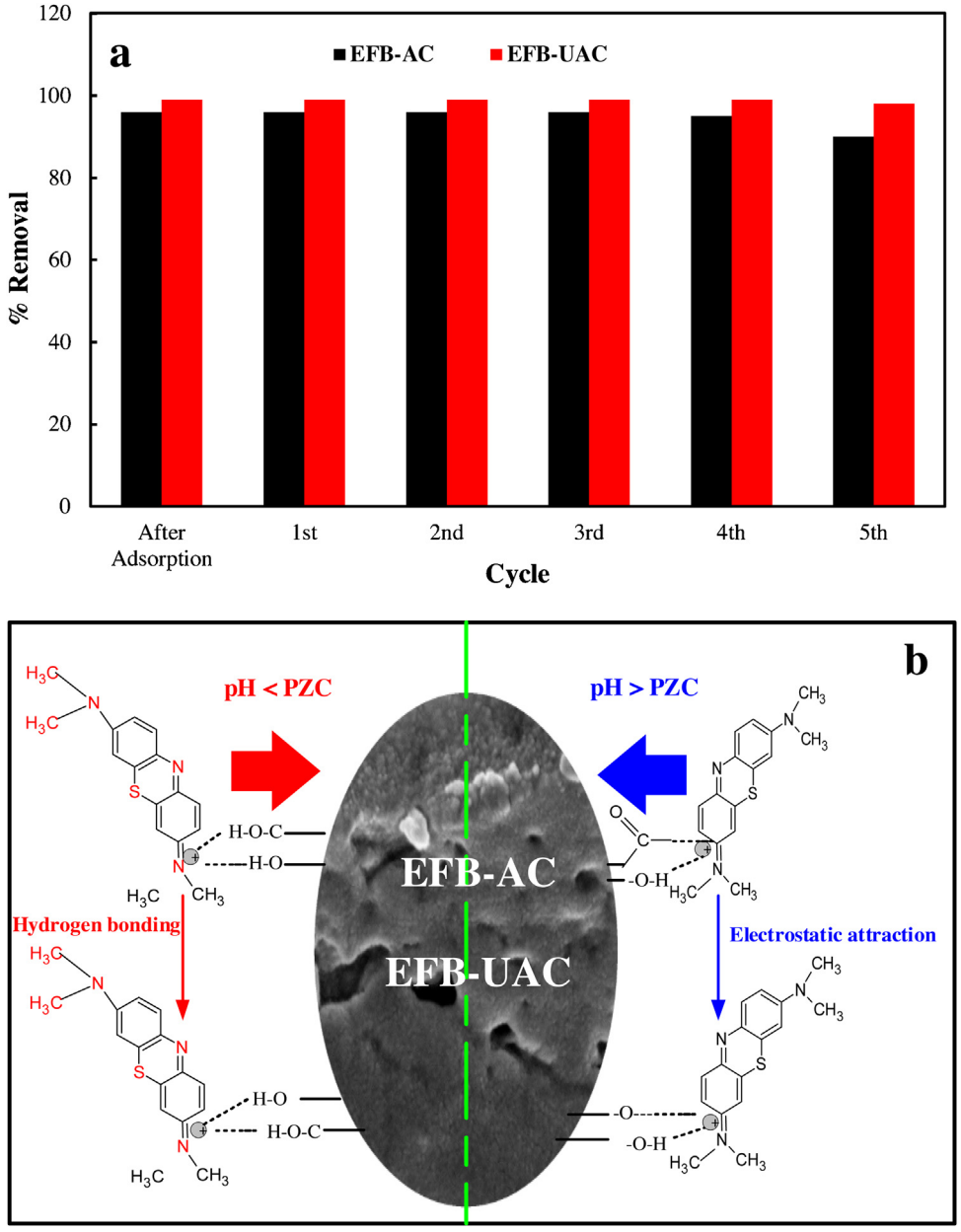

Fig. 7 – (a) Reusability studies of EFB-AC and EFB-UAC (b) schematic demonstration adsorption mechanism of MB on the surface of EFB-AC and EFB-UAC.

than desorption phenomenon, thereby indicating high affinity between MB molecules and the activated carbon.

3.8. *Adsorption thermodynamics*

Thermodynamic plots for MB adsorption onto EFB-AC and EFB-UAC are shown in Figs. S5 and S6, while the calculated parameters are presented in Table 8. According to Table 8, it can be observed that the values of ΔG° increased from 1141.94 to 1995.78 kJ/mol and 1744.31 to 3008.56 kJ/mol for adsorption of MB by EFB-AC and EFB-UAC, respectively at different temperatures. The adsorption energy increased with temperature because of the endothermic nature of MB adsorption. Hence, temperature increase translated to decrease in the solution viscosity, while the kinetic energy and diffusion rate of the MB molecules increased onto the active sites of the adsorbents (Mechi et al., 2019). In addition, it was observed that EFB-UAC had higher adsorption energy, therefore the affinity

of the active sites of the EFB-UAC surface to the MB molecule is more significant than the EPB-AC sites due to lower interaction of MB molecules with EFB-AC compared to the MB/EFB-UAC.

As shown in Table 8, values of ΔH° for MB adsorption did not fall within 1–40 kJ/mol that indicates adsorption by physisorption (Cheng et al., 2017). This suggests that the adsorption of MB by the two materials was chemisorption in nature. However, the results of ΔH° obtained in this study for both EFB-AC and EFB-UAC are 288.09 and 480.07 kJ/mol, thus confirmed that the adsorption between the MB molecule and the active sites of EFB-AC or EFB-UAC was more of chemisorption than physisorption. Also, the positive values of ΔH° demonstrated the endothermic characteristic of MB adsorption. The negative values of ΔS° revealed decrease in randomness at the interface of the adsorbent-MB solution (Li et al., 2018), thereby showing a more ordered transition state than the initial state.

3.9. *Reusability*

Regeneration capacity of the adsorbents has been identified as a major parameter for economical and valuable environmental application. The result of the desorption cycles of EFB-AC and EFB-UAC shown in Fig. 7(a) revealed that the regenerated adsorbents can be reused for at least four (EFB-AC) and five (EFB-UAC) adsorption–desorption cycles without change in its effectiveness. However, decrease in the efficiency of EFB-AC observed beyond the 4th cycle could be attributable to the deposition of MB molecules on the EFB-AC surface during the process of regeneration. The effectiveness of EFB-UAC over EFB-AC could be linked to the ultrasonic effect during the activation process of the activated EFB.

3.10. *Adsorption mechanism*

There are several parameters influencing the adsorption process; including the surface chemistry of the materials, molecular structure of dye and the adsorbate interactions (Wang et al., 2019), In this study, MB adsorption was highly dependent on the pH and ionic strength. Fig. 7(b) provides an idea concerning the mechanism of MB adsorption onto the adsorbents. The MB adsorption onto EFB-AC and EFB-UAC was favored by high pH ($pH > pH_{PZC}$) values which resulted to high amount of MB adsorbed. This was ascribed to strong intermolecular electrostatic attraction between the negatively charged adsorbent (EFB-AC and EFB-UAC) surface and the positively charged MB solution. However, at lower pH ($pH < pH_{PZC}$), a small amount of MB was adsorbed by EFB-AC and EFB-UAC due to positive surface nature of the adsorbent which did not enhance MB adsorption because of electrostatic repulsion (Miyah et al., 2018). Other adsorption mechanisms instead of electrostatic interactions may also be responsible for MB adsorption onto the adsorbents (Wang et al., 2018c). Also, the presence of hydrogen bond between nitrogen of MB and hydroxyl of EFB-AC and EFB-UAC could be attributable to the adsorption of MB molecule (Cheng et al., 2017). The investigation of salt effect showed that increasing the ionic strength, decreased the MB adsorption capacity onto the adsorbents which validates the existence of electrostatic attraction between the adsorbents and the MB molecule (Lu et al., 2019).

4. Conclusion

The prepared EFB-AC and EFB-UAC from EFB were successfully applied to adsorb MB from aqueous solution under ultrasonic influence. The study showed that EFB-AC has a surface area of 1036 m^2/g, while EFB-UAC has a higher surface area of 2114 m^2/g. The characterization of EFB-AC and EFB-UAC using BET, TGA, HRSEM, XRD, FTIR and XPS showed that EFB-UAC has high surface area, better thermal stability, better pores development and improved surface chemistry compared to the EFB-AC due to the influence of sonication. The obtained high surface area and mesopores of EFB-UAC facilitated the adsorption of MB molecules at the optimum conditions: pH (10), adsorbent dosage (30 mg), sonication time (40 min). temperature (50 °C) and MB initial concentration (50 mg/L). The equilibrium data was best described by the Langmuir model, indicating that MB adsorption predominantly occurred due to strong interactions between the adsorbents (EFB-AC and EFB-UAC) and MB. The maximum monolayer adsorption capacity was shown to be 400 and 435 mg/g for the adsorption of MB onto EFB-AC and EFB-UAC respectively. The adsorption kinetics was best described by the pseudo-second order kinetic model. The thermodynamic parameters validated that the adsorption of MB is endothermic in nature and favored by chemisorption. The EFB-AC and EFB-UAC had reusability potentials for at least four and five cycles without decrease in the removal efficiency. The findings of this study suggest that the developed EFB-UAC adsorbents showed high efficiency using sonication assisted adsorption of MB and has great potential for application in the removal of organic pollutants. Future work includes the analysis of the actual cost and valuation of the life cycle for the entire process could be studied for possible application in the industry.

Conflicting interests declaration

The author(s) declared no potential conflicts of interest.

Acknowledgements

This work was financially supported by the Petroleum Technology Development Fund of Nigeria (grant number PTDF/ED/LSS/PhD/TCE/123/17). The authors also appreciate the management of Centre for Genetic Engineering and Biotechnology (CGEB), Federal University of Technology, Minna, Nigeria for making the necessary facilities available for this research. The contributions of Prof. W.D. Roos of Department of Physics, University of the Free State, Bloemfontein, South Africa in the XPS analysis of the samples and proofreading this work is equally appreciated.

Appendix A. Supplementary data

Supplementary material related to this article can be found, in the online version, at doi:https://doi.org/10.1016/j.cherd.2019.10.016.

References

Ait Ahsaaine, H., Zbair, M., Anfar, Z., Naciri, Y., El haouti, R., El Alem, N., Ezahri, M., 2018. Cationic dyes adsorption onto high surface area 'almond shell' activated carbon: kinetics, equilibrium isotherms and surface statistical modeling.

Mater. Today Chem. 8, 121–132, http://dx.doi.org/10.1016/j.mtchem.2018.03.004.
Altıntıg, E., Altundag, H., Tuzen, M., Sarı, A., Sarı, A., 2017. Effective removal of methylene blue from aqueous solutions using magnetic loaded activated carbon as novel adsorbent. Chem. Eng. Res. Des. 122, 151–163, http://dx.doi.org/10.1016/j.cherd.2017.03.035.
Banerjee, P., Barman, S.R., Mukhopadhayay, A., Das, P., 2017. Ultrasound assisted mixed azo dye adsorption by chitosan–graphene oxide nanocomposite. Chem. Eng. Res. Des. 117, 43–56, http://dx.doi.org/10.1016/j.cherd.2016.10.009.
Bankole, M.T., Abdulkareem, A.S., Mohammed, I.A., Ochigbo, S.S., Tijani, J.O., Abubakre, O.K., Roos, W.D., 2019. Selected heavy metals removal from electroplating wastewater by purified and polyhydroxylbutyrate functionalized carbon nanotubes adsorbents. Sci. Rep. 9, 1–19, http://dx.doi.org/10.1038/s41598-018-37899-4.
Cai, W., Li, Z., Wei, J., Liu, Y., 2018. Synthesis of peanut shell based magnetic activated carbon with excellent adsorption performance towards electroplating wastewater. Chem. Eng. Res. Des. 140, 23–32, http://dx.doi.org/10.1016/j.cherd.2018.10.008.
Charola, S., Patel, H., Chandna, S., Maiti, S., 2019. Optimization to prepare porous carbon from mustard husk using response surface methodology adopted with central composite design. J. Clean. Prod. 223, 969–979, http://dx.doi.org/10.1016/j.jclepro.2019.03.169.
Chen, H., Chen, Z., Zhao, G., Zhang, Z., Xu, C., Liu, Y., Chen, J., Zhuang, L., Haya, T., Wang, X., 2018. Enhanced adsorption of U(VI) and241Am(III) from wastewater using Ca/Al layered double hydroxide@carbon nanotube composites. J. Hazard. Mater. 347, 67–77, http://dx.doi.org/10.1016/j.jhazmat.2017.12.062.
Cheng, S., Zhang, L., Ma, A., Xia, H., Peng, J., Li, C., Shu, J., 2018. Comparison of activated carbon and iron/cerium modified activated carbon to remove methylene blue from wastewater. J. Environ. Sci. (China) 65, 92–102, http://dx.doi.org/10.1016/j.jes.2016.12.027.
Cheng, S., Zhang, L., Xia, H., Peng, J., Shu, J., Li, C., Jiang, X., Zhang, Q., 2017. Adsorption behavior of methylene blue onto waste-derived adsorbent and exhaust gases recycling. RSC Adv. 7, 27331–27341, http://dx.doi.org/10.1039/c7ra01482a.
Danish, M., Ahmad, T., Hashim, R., Said, N., Akhtar, M.N., Mohamad-Saleh, J., Sulaiman, O., 2018a. Comparison of surface properties of wood biomass activated carbons and their application against rhodamine B and methylene blue dye. Surf. Interfaces, http://dx.doi.org/10.1016/j.surfin.2018.02.001, Elsevier B.V.
Danish, M., Ahmad, T., Majeed, S., Ahmad, M., Ziyang, L., Pin, Z., Shakeel Iqubal, S.M., 2018b. Use of banana trunk waste as activated carbon in scavenging methylene blue dye: kinetic, thermodynamic, and isotherm studies. Bioresour. Technol. Rep. 3, 127–137, http://dx.doi.org/10.1016/j.biteb.2018.07.007.
Dissanayake Herath, G.A., Poh, L.S., Ng, W.J., 2019. Statistical optimization of glyphosate adsorption by biochar and activated carbon with response surface methodology. Chemosphere, 533–540, http://dx.doi.org/10.1016/j.chemosphere.2019.04.078.
Dubinin, M.M., 1969. The potential theory of adsorption of gas theory of adsorption of gases and vapour. Chem. Rev. 60, 235–241.
El-Shafey, E.I., Ali, S.N.F., Al-Busafi, S., Al-Lawati, H.A.J., 2016. Preparation and characterization of surface functionalized activated carbons from date palm leaflets and application for methylene blue removal. J. Environ. Chem. Eng. 4, 2713–2724, http://dx.doi.org/10.1016/j.jece.2016.05.015.
Fakhri, H., Mahjoub, A.R., Aghayan, H., 2017. Effective removal of methylene blue and cerium by a novel pair set of heteropoly acids based functionalized graphene oxide: adsorption and photocatalytic study. Chem. Eng. Res. Des. 120, 303–315, http://dx.doi.org/10.1016/j.cherd.2017.02.030.
Franciski, M.A., Peres, E.C., Godinho, M., Perondi, D., Foletto, E.L., Collazzo, G.C., Dotto, G.L., 2018. Development of CO2 activated biochar from solid wastes of a beer industry and its application for methylene blue adsorption. Waste Manag. 78, 630–638, http://dx.doi.org/10.1016/j.wasman.2018.06.040.
Garba, Z.N., Rahim, A.A., 2014. Process optimization of $K_2C_2O_4$ -activated carbon from Prosopis Africana seed hulls using response surface methodology. J. Anal. Appl. Pyrolysis 107, 306–312, http://dx.doi.org/10.1016/j.jaap.2014.03.016.
Gaur, N., Narasimhulu, K., PydiSetty, Y., 2018. Recent advances in the bio-remediation of persistent organic pollutants and its effect on environment. J. Clean. Prod. 198, 1602–1631, http://dx.doi.org/10.1016/j.jclepro.2018.07.076.
Guo, Q., Liu, Y., Qi, G., Jiao, W., 2019. Adsorption and desorption behaviour of toluene on activated carbon in a high gravity rotating bed. Chem. Eng. Res. Des. 143, 47–55, http://dx.doi.org/10.1016/j.cherd.2019.01.005.
Hassan, A.F., Elhadidy, H., 2017. Production of activated carbons from waste carpets and its application in methylene blue adsorption: Kinetic and thermodynamic studies. J. Environ. Chem. Eng. 5, 955–963, http://dx.doi.org/10.1016/j.jece.2017.01.003.
Ho, Y.S., McKay, G., 1999. Pseudo-second order model for sorption processes. Process. Biochem. 34, 451–465, http://dx.doi.org/10.1016/S0032-9592(98)00112-5.
Ho, Y.S., McKay, G., 1998. Sorption of dye from aqueous solution by peat. Chem. Eng. J. 70, 115–124, http://dx.doi.org/10.1016/S1385-8947(98)00076-X.
Hodaifa, G., Gallardo, P.A.R., García, C.A., Kowalska, M., Seyedsalehi, M., 2019. Chemical oxidation methods for treatment of real industrial olive oil mill wastewater. J. Taiwan Inst. Chem. Eng., 1–8, http://dx.doi.org/10.1016/j.jtice.2019.02.001.
Ibupoto, A.S., Qureshi, U.A., Ahmed, F., Khatri, Z., Khatri, M., Maqsood, M., Brohi, R.Z., Kim, I.S., 2018. Reusable carbon nanofibers for efficient removal of methylene blue from aqueous solution. Chem. Eng. Res. Des. 136, 744–752, http://dx.doi.org/10.1016/j.cherd.2018.06.035.
Islam, M.A., Ahmed, M.J., Khanday, W.A., Asif, M., Hameed, B.H., 2017. Mesoporous activated coconut shell-derived hydrochar prepared via hydrothermal carbonization-NaOH activation for methylene blue adsorption. J. Environ. Manage. 203, 237–244, http://dx.doi.org/10.1016/j.jenvman.2017.07.029.
Jiang, X., Xia, H., Zhang, L., Cheng, S., Zhang, Q., Chen, Q., Hu, W., 2018. Synthesis of copper-loaded activated carbon for enhancing the photocatalytic removal of methylene blue. J. Mol. Liq. 272, 353–360, http://dx.doi.org/10.1016/j.molliq.2018.09.087.
Kazak, O., Eker, Y.R., Bingol, H., Tor, A., 2018. Preparation of chemically-activated high surface area carbon from waste vinasse and its efficiency as adsorbent material. J. Mol. Liq. 272, 189–197, http://dx.doi.org/10.1016/j.molliq.2018.09.085.
Kazak, O., Eker, Y.R., Bingol, H., Tor, A., 2017. Novel preparation of activated carbon by cold oxygen plasma treatment combined with pyrolysis. Chem. Eng. J, 1–40, http://dx.doi.org/10.1016/j.cej.2017.05.107.
Khalil, K.M.S., Allam, O.A.S., Khairy, M., Mohammed, K.M.H., Elkhatib, R.M., Hamed, M.A., 2017. High surface area nanostructured activated carbons derived from sustainable sorghum stalk. J. Mol. Liq. 247, 386–396, http://dx.doi.org/10.1016/j.molliq.2017.09.090.
Kluczka, J., Pudło, W., Krukiewicz, K., 2019. Boron adsorption removal by commercial and modified activated carbons. Chem. Eng. Res. Des. 147, 30–42, http://dx.doi.org/10.1016/j.cherd.2019.04.021.
Konicki, W., Aleksandrzak, M., Mijowska, E., 2017. Equilibrium, kinetic and thermodynamic studies on adsorption of cationic dyes from aqueous solutions using graphene oxide. Chem. Eng. Res. Des. 123, 35–49, http://dx.doi.org/10.1016/j.cherd.2017.03.036.
Konicki, W., Hełminiak, A., Arabczyk, W., Mijowska, E., 2018. Adsorption of cationic dyes onto Fe@graphite core–shell magnetic nanocomposite: equilibrium, kinetics and thermodynamics. Chem. Eng. Res. Des. 129, 259–270, http://dx.doi.org/10.1016/j.cherd.2017.11.004.

Langmuir, I., 1918. The adsorption of gases on plane surfaces of glass, mica and platinum. J. Am. Chem. Soc. 40, 1361–1403, http://dx.doi.org/10.1021/ja02242a004.
Lee, J., Kim, K.H., Kwon, E.E., 2017. Biochar as a catalyst. Renew. Sustain. Energy Rev. 77, 70–79, http://dx.doi.org/10.1016/j.rser.2017.04.002.
Li, K., Zhou, M., Liang, L., Jiang, L., Wang, W., 2019. Ultrahigh-surface-area activated carbon aerogels derived from glucose for high-performance organic pollutants adsorption. J. Colloid Interface Sci. 546, 333–343, http://dx.doi.org/10.1016/j.jcis.2019.03.076.
Li, S., Han, K., Li, J., Li, M., Lu, C., 2017a. Preparation and characterization of super activated carbon produced from gulfweed by KOH activation. Microporous Mesoporous Mater. 243, 291–300, http://dx.doi.org/10.1016/j.micromeso.2017.02.052.
Li, Z., Wang, G., Zhai, K., He, C., Li, Q., Guo, P., 2018. Methylene blue adsorption from aqueous solution by loofah sponge-based porous carbons. Colloids Surf. A Physicochem. Eng. Aspect 538, 28–35, http://dx.doi.org/10.1016/j.colsurfa.2017.10.046.
Li, W., Zuo, P., Xu, D., Xu, Y., Wang, K., Bai, Y., Ma, H., 2017b. Tunable adsorption properties of bentonite/carboxymethyl cellulose-g-poly(2-(dimethylamino) ethyl methacrylate) composites toward anionic dyes. Chem. Eng. Res. Des. 124, 260–270, http://dx.doi.org/10.1016/j.cherd.2017.06.034.
Liew, R.K., Nam, W.L., Chong, M.Y., Phang, X.Y., Su, M.H., Nai, P., Yek, Y., Ma, N.L., Cheng, C.K., Chong, C.T., Lam, S.S., 2017. Oil palm waste: an abundant and promising feedstock for microwave pyrolysis conversion into good quality biochar with potential multi-applications. Process Saf. Environ. Prot., 1–39, http://dx.doi.org/10.1016/j.psep.2017.10.005.
Lima, H.H.C., Maniezzo, R.S., Llop, M.E.G., Kupfer, V.L., Arroyo, P.A., Guilherme, M.R., Rubira, A.F., Girotto, E.M., Rinaldi, A.W., 2019. Synthesis and characterization of pecan nutshell-based adsorbent with high specific area and high methylene blue adsorption capacity. J. Mol. Liq. 276, 570–576, http://dx.doi.org/10.1016/j.molliq.2018.12.010.
Lin, G., Wang, S., Zhang, L., Hu, T., Peng, J., Cheng, S., Fu, L., 2018. Synthesis and evaluation of thiosemicarbazide functionalized corn bract for selective and efficient adsorption of Au(III) from aqueous solutions. J. Mol. Liq. 258, 235–243, http://dx.doi.org/10.1016/j.molliq.2018.03.030.
Lu, K., Wang, T., Zhai, L., Wu, W., Dong, S., Gao, S., Mao, L., 2019. Adsorption behavior and mechanism of Fe-Mn binary oxide nanoparticles: adsorption of methylene blue. J. Colloid Interface Sci. 539, 553–562, http://dx.doi.org/10.1016/j.jcis.2018.12.094.
Ma, Z., Yang, Y., Ma, Q., Zhou, H., Luo, X., Liu, X., Wang, S., 2017. Evolution of the chemical composition, functional group, pore structure and crystallographic structure of bio-char from palm kernel shell pyrolysis under different temperatures. J. Anal. Appl. Pyrolysis, 1–38, http://dx.doi.org/10.1016/j.jaap.2017.07.015.
Marrakchi, F., Bouaziz, M., Hameed, B.H., 2017. Adsorption of acid blue 29 and methylene blue on mesoporous K2CO3-activated olive pomace boiler ash. Colloids Surf. A Physicochem. Eng. Aspect 535, 157–165, http://dx.doi.org/10.1016/j.colsurfa.2017.09.014.
Mechi, N., Ben Khemis, I., Dotto, G.L., Franco, D., Sellaoui, L., Ben Lamine, A., 2019. Investigation of the adsorption mechanism of methylene blue (MB) on Cortaderia selloana flower spikes (FSs) and on Cortaderia selloana flower spikes derived carbon fibers (CFs). J. Mol. Liq. 280, 268–273, http://dx.doi.org/10.1016/j.molliq.2019.02.024.
Menya, E., Olupot, P.W., Storz, H., Lubwama, M., Kiros, Y., 2017. Production and performance of activated carbon from rice husks for removal of natural organic matter from water: a review. Chem. Eng. Res. Des., http://dx.doi.org/10.1016/j.cherd.2017.11.008.
Miyah, Y., Lahrichi, A., Idrissi, M., Khalil, A., Zerrouq, F., 2018. Adsorption of methylene blue dye from aqueous solutions onto walnut shells powder: equilibrium and kinetic studies. Surf. Interfaces 11, 74–81, http://dx.doi.org/10.1016/j.surfin.2018.03.006.
Moralı, U., Demiral, H., Şensöz, S., 2018. Optimization of activated carbon production from sunflower seed extracted meal: taguchi design of experiment approach and analysis of variance. J. Clean. Prod. 189, 602–611, http://dx.doi.org/10.1016/j.jclepro.2018.04.084.
Morin, M., Pécate, S., Hémati, M., 2018. Experimental study and modelling of the kinetic of biomass char gasification in a fluidized bed reactor. Chem. Eng. Res. Des. 131, 488–505, http://dx.doi.org/10.1016/j.cherd.2017.09.030.
Mouni, L., Belkhiri, L., Bollinger, J.C., Bouzaza, A., Assadi, A., Tirri, A., Dahmoune, F., Madani, K., Remini, H., 2018. Removal of methylene blue from aqueous solutions by adsorption on Kaolin: kinetic and equilibrium studies. Appl. Clay Sci. 153, 38–45, http://dx.doi.org/10.1016/j.clay.2017.11.034.
Nasrullah, A., Saad, B., Bhat, A.H., Khan, A.S., Danish, M., Isa, M.H., Naeem, A., 2019. Mangosteen peel waste as a sustainable precursor for high surface area mesoporous activated carbon: characterization and application for methylene blue removal. J. Clean. Prod. 211, 1190–1200, http://dx.doi.org/10.1016/j.jclepro.2018.11.094.
Novais, R.M., Caetano, A.P.F., Seabra, M.P., Labrincha, J.A., Pullar, R.C., 2018. Extremely fast and efficient methylene blue adsorption using eco-friendly cork and paper waste-based activated carbon adsorbents. J. Clean. Prod. 197, 1137–1147, http://dx.doi.org/10.1016/j.jclepro.2018.06.278.
Pinto, M.B., Samanamud, G.R.L., Baston, E.P., França, A.B., Naves, L.L.R., Loures, C.C.A., Naves, F.L., 2019. Multivariate and multiobjective optimization of tannery industry effluent treatment using Musa sp flower extract in the coagulation and flocculation process. J. Clean. Prod. 219, 655–666, http://dx.doi.org/10.1016/j.jclepro.2019.02.060.
Qasim, M., Badrelzaman, M., Darwish, N.N., Darwish, N.A., Hilal, N., 2019. Reverse osmosis desalination: a state-of-the-art review. Desalination 459, 59–104, http://dx.doi.org/10.1016/j.desal.2019.02.008.
Schüler, C., Betzenbichler, F., Drescher, C., Hinrichsen, O., 2018. Optimization of the synthesis of Ni catalysts via chemical vapor deposition by response surface methodology. Chem. Eng. Res. Des. 132, 303–312, http://dx.doi.org/10.1016/j.cherd.2018.01.015.
Shu, J., Liu, R., Wu, H., Liu, Z., Sun, X., Tao, C., 2018. Adsorption of methylene blue on modified electrolytic manganese residue: kinetics, isotherm, thermodynamics and mechanism analysis. J. Taiwan Inst. Chem. Eng. 82, 351–359, http://dx.doi.org/10.1016/j.jtice.2017.11.020.
Sodeifian, G., Ali, S., 2018. Utilization of ultrasonic-assisted RESOLV (US-RESOLV) with polymeric stabilizers for production of amiodarone hydrochloride nanoparticles: optimization of the process. Chem. Eng. Res. Des. 142, 268–284, http://dx.doi.org/10.1016/j.cherd.2018.12.020.
Sulaiman, N.S., Hashim, R., Mohamad Amini, M.H., Danish, M., Sulaiman, O., 2018. Optimization of activated carbon preparation from cassava stem using response surface methodology on surface area and yield. J. Clean. Prod. 198, 1422–1430, http://dx.doi.org/10.1016/j.jclepro.2018.07.061.
Suresh, A., Grygolowicz-Pawlak, E., Pathak, S., Poh, L.S, Abdul Majid, M. bin, Dominiak, D., Bugge, T.V., Gao, X., Ng, W.J., 2018. Understanding and optimization of the flocculation process in biological wastewater treatment processes: a review. Chemosphere 210, 401–416, http://dx.doi.org/10.1016/j.chemosphere.2018.07.021.
Tian, D., Xu, Z., Zhang, D., Chen, W., Cai, J., Deng, H., Sun, Z., Zhou, Y., 2019. Micro–mesoporous carbon from cotton waste activated by FeCl3/ZnCl2: preparation, optimization, characterization and adsorption of methylene blue and eriochrome black T. J. Solid State Chem. 269, 580–587, http://dx.doi.org/10.1016/j.jssc.2018.10.035.
Tian, G., Wang, W., Zhu, Y., Zong, L., Kang, Y., Wang, A., 2018. Carbon/Attapulgite composites as recycled palm oil-decoloring and dye adsorbents. Materials (Basel) 11, 1–16, http://dx.doi.org/10.3390/ma11010086.

United States Department of Agriculture, 2019. World agricultural production. Circ. Ser. (May), 6–15.

Wang, B., Gao, B., Zimmerman, A.R., Lee, X., 2018a. Impregnation of multiwall carbon nanotubes in alginate beads dramatically enhances their adsorptive ability to aqueous methylene blue. Chem. Eng. Res. Des. 133, 235–242, http://dx.doi.org/10.1016/j.cherd.2018.03.026.

Wang, R., Yu, J., Hao, Q., 2018b. Activated carbon/Mn 0.6 Zn 0.4 Fe 2 O 4 composites: facile synthesis, magnetic performance and their potential application for the removal of methylene blue from water. Chem. Eng. Res. Des. 132, 215–225, http://dx.doi.org/10.1016/j.cherd.2018.01.027.

Wang, Y., Zhang, Y., Li, S., Zhong, W., Wei, W., 2018c. Enhanced methylene blue adsorption onto activated reed-derived biochar by tannic acid. J. Mol. Liq. 268, 658–666, http://dx.doi.org/10.1016/j.molliq.2018.07.085.

Wang, N., Chen, J., Wang, J., Feng, J., Yan, W., 2019. Removal of methylene blue by Polyaniline/TiO 2 hydrate: adsorption kinetic, isotherm and mechanism studies. Powder Technol. 347, 93–102, http://dx.doi.org/10.1016/j.powtec.2019.02.049.

Xu, W., Zhao, Q., Wang, R., Jiang, Z., Zhang, Z., Gao, X., Ye, Z., 2017. Optimization of organic pollutants removal from soil eluent by activated carbon derived from peanut shells using response surface methodology. Vacuum 141, 307–315, http://dx.doi.org/10.1016/j.vacuum.2017.04.031.

Yang, J., Chen, Y., Xu, P., Li, Y., Jia, X., Song, H., 2019. Fabrication of compressible and underwater superoleophobic carbon/g-C3N4 aerogel for wastewater purification. Mater. Lett. 254, 210–213, http://dx.doi.org/10.1016/j.matlet.2019.07.069.

Yu, Q., Zhao, Huirong, Zhao, Hong, Sun, S., Ji, X., Li, M., Wang, Y., 2019. Preparation of tobacco-stem activated carbon from using response surface methodology and its application for water vapor adsorption in solar drying system. Sol. Energy 177, 324–336, http://dx.doi.org/10.1016/j.solener.2018.11.029.

Zbair, Ait, Ahsaine, H., Anfar, Z., 2018. Porous carbon by microwave assisted pyrolysis: an effective and low-cost adsorbent for sulfamethoxazole adsorption and optimization using response surface methodology. J. Clean. Prod. 202, 571–581, http://dx.doi.org/10.1016/j.jclepro.2018.08.155.

Zhang, B., Han, X., Gu, P., Fang, S., Bai, J., 2017. Response surface methodology approach for optimization of ciprofloxacin adsorption using activated carbon derived from the residue of desilicated rice husk. J. Mol. Liq. 238, 316–325, http://dx.doi.org/10.1016/j.molliq.2017.04.022.

Zhang, C., Li, P., Huang, W., Cao, B., 2016. Selective adsorption and separation of organic dyes in aqueous solutions by hydrolyzed PIM-1 microfibers. Chem. Eng. Res. Des. 109, 76–85, http://dx.doi.org/10.1016/j.cherd.2016.01.006.

Zhang, X., Cheng, L., Wu, X., Tang, Y., Wu, Y., 2015. Activated carbon coated palygorskite as adsorbent by activation and its adsorption for methylene blue. J. Environ. Sci. (China) 33, 97–105, http://dx.doi.org/10.1016/j.jes.2015.01.014.